

2P-NucTag: on-demand phototagging for molecular analysis of functionally identified cortical neurons

Authors: Jingcheng Shi^{1,2,3,*}, Boaz Nutkovich^{5,6,*}, Dahlia Kushinsky^{5,6,*}, Bovey Y. Rao^{1,2,3,*}, Stephanie A. Herrlinger^{1,2,*}, Emmanouil Tsivourakis^{4,5,6}, Tiberiu S. Mihaila^{1,2}, Margaret E. Conde Paredes^{1,2,3,7}, Katayun Cohen-Kashi Malina^{5,6}, Cliodhna K. O'Toole^{1,2}, Hyun Choong Yong^{1,2}, Brynn M. Sanner^{1,2}, Angel Xie^{1,2}, Erdem Varol⁷, Attila Losonczy^{1,2,#,‡}, and Ivo Spiegel^{5,6,#,‡}

Affiliations:

¹ Department of Neuroscience, Columbia University, New York, NY, United States

² Mortimer B. Zuckerman Mind Brain Behavior Institute, Columbia University, New York, NY, United States

³ Doctoral Program in Neurobiology and Behavior, Columbia University, New York, NY, United States

⁴ Stavros Niarchos Foundation Center for Precision Psychiatry and Mental Health, New York, NY, United States

⁵ Department of Brain Sciences, Weizmann Institute of Science, Rehovot, Israel

⁶ Department of Molecular Neuroscience, Weizmann Institute of Science, Rehovot, Israel

⁷ Tandon School of Engineering, New York University, New York, NY, United States

* Co-first authors

Co-senior authors

‡ Corresponding authors. Emails: al2856@columbia.edu, ivo.spiegel@weizmann.ac.il

Summary:

Neural circuits are characterized by genetically and functionally diverse cell types. A mechanistic understanding of circuit function is predicated on linking the genetic and physiological properties of individual neurons. However, it remains highly challenging to map the molecular properties onto functionally heterogeneous neuronal subtypes in mammalian cortical circuits *in vivo*. Here, we introduce a high-throughput two-photon nuclear phototagging (2P-NucTag) approach for on-demand and indelible labeling of single neurons via a photoactivatable red fluorescent protein following *in vivo* functional characterization in behaving mice. Using this novel function-forward pipeline to selectively label and transcriptionally profile previously inaccessible ‘place’ and ‘silent’ cells in the hippocampus of behaving mice, we identify unexpected differences in gene expression between these hippocampal pyramidal neurons with distinct spatial coding properties. Thus, 2P-NucTag opens a new way to uncover the molecular principles that govern the functional organization of neural circuits.

One-Sentence Summary: 2P-NucTag - A novel high-throughput on-demand phototagging approach to identify selective gene expression of functionally distinct neurons *in vivo* in behaving animals.

1 **Introduction**

2
3 Information processing in neural circuits requires precise interactions between molecularly and
4 functionally diverse populations of neurons. Since gene expression dictates neuronal connectivity
5 and function, a fundamental goal of neuroscience has been to characterize gene expression profiles
6 of functionally defined neurons and to measure changes in gene expression associated with distinct
7 functional states of neurons¹. High-throughput transcriptomic approaches such as single-cell-/
8 nucleus RNA-sequencing (sc/snRNA-seq) and spatial transcriptomics have greatly accelerated the
9 identification of gene programs in molecularly distinct types of neurons at single-cell resolution^{2–}
10 ⁸. However, functional and anatomical characterization of such molecularly identified neuronal
11 subtypes^{9–13} remains highly challenging as it requires the generation and validation of new
12 subtype-specific molecular tools^{14–16}. Recently, correlated *in vivo* Ca²⁺ imaging with *post hoc*
13 spatial transcriptomics (ST) has been used to relate gene expression with *in vivo* function^{17–20}, but
14 this approach is limited by the relatively low density of the cells investigated and by the number
15 of genes that can be probed in ST experiments. Furthermore, this approach is not suitable for
16 unbiased transcriptomic analyses as selecting probes for ST requires prior knowledge of the genes
17 of interest. Therefore, a method for unbiased identification of genes that are differentially
18 expressed in densely packed, functionally distinct glutamatergic pyramidal neurons (PNs) would
19 significantly accelerate our understanding of how gene expression determines circuit function and
20 behavior.

21 The inability to tag single functionally identified cortical PNs *in vivo* in behaving animals
22 presents a significant challenge as large-scale neural recordings have shown that PNs are highly
23 heterogeneous in their physiological, anatomical, and response properties, and are spatially
24 intermixed within neocortical and hippocampal circuits^{16,21–27}. For example, PNs with distinct
25 spatial coding properties are distributed throughout the dense cell body layer of the hippocampus^{28–}
26 ³⁵. However, the origin of this functional diversity in feature selectivity is largely unknown, and it
27 remains unclear if gene expression differences are associated with discrete and transient functional
28 cell states^{35–40}. Thus, there is a critical need for function-forward approaches to directly identify
29 the transcriptional profiles of cortical neurons that were functionally characterized *in vivo* in
30 behaving animals, and to test subsequently whether the functional differences between seemingly
31 identical neurons are indeed driven by specific differentially expressed genes.

32 Previous attempts using Ca²⁺ and light-dependent labeling of transiently active
33 neurons^{16,41–43} were limited by their spatial resolution, deficiencies in targeting neurons with high
34 baseline intracellular Ca²⁺ levels, and the inability to label neurons that decrease their activity in
35 response to behavioral state or sensory stimuli. Similarly, labeling approaches based on the
36 expression of immediate early genes^{44–47} lack the temporal and spatial resolution to faithfully
37 report the precise activity patterns and response properties of single neurons that are active but
38 functionally distinct (e.g., neurons with different response tuning properties or feature selectivity).
39 Finally, previous attempts to tag cortical neurons with photoactivatable fluorescent proteins⁴⁸ with
40 single-cell precision have been deployed with limited success⁴⁹. Thus, although these methods,
41 collectively, have contributed greatly to the understanding of how co-active cells contribute to
42 behavior and cognition, there is an unmet need for an approach that allows for identifying the
43 molecular and cellular properties of single neurons that were functionally characterized *in vivo*
44 based on their precise activity patterns in behaving animals.

45 Here we introduce 2P-NucTag, a robust *in vivo* pipeline for in-depth molecular and cellular
46 analyses of single neurons that were functionally characterized in behaving animals. The 2P-

47 NucTag approach optimizes a previously described *ex vivo* framework⁵⁰ and is based on the co-
48 expression of a photoactivatable red fluorescent protein (PAmCherry) and a genetically encoded
49 green Ca^{2+} indicator (GCaMP7f or GCaMP8s) - thereby, 2P-NucTag allows for combining large-
50 scale *in vivo* two-photon (2P) functional imaging of cortical PNs with reliable and selective 2P
51 phototagging of the nuclei of single neurons based on their functional properties as well as with
52 *post-hoc* in-depth unbiased transcriptomics and cellular analyses of the photolabeled neurons.
53 Using this novel approach, we identify unexpected differences in gene expression and cellular
54 properties in previously inaccessible ‘place’ and ‘silent’ cells in the hippocampus of behaving
55 mice. Thus, we achieve previously unattainable molecular characterization of functionally
56 identified PNs *in vivo* in behaving animals using the 2P-NucTag approach.
57

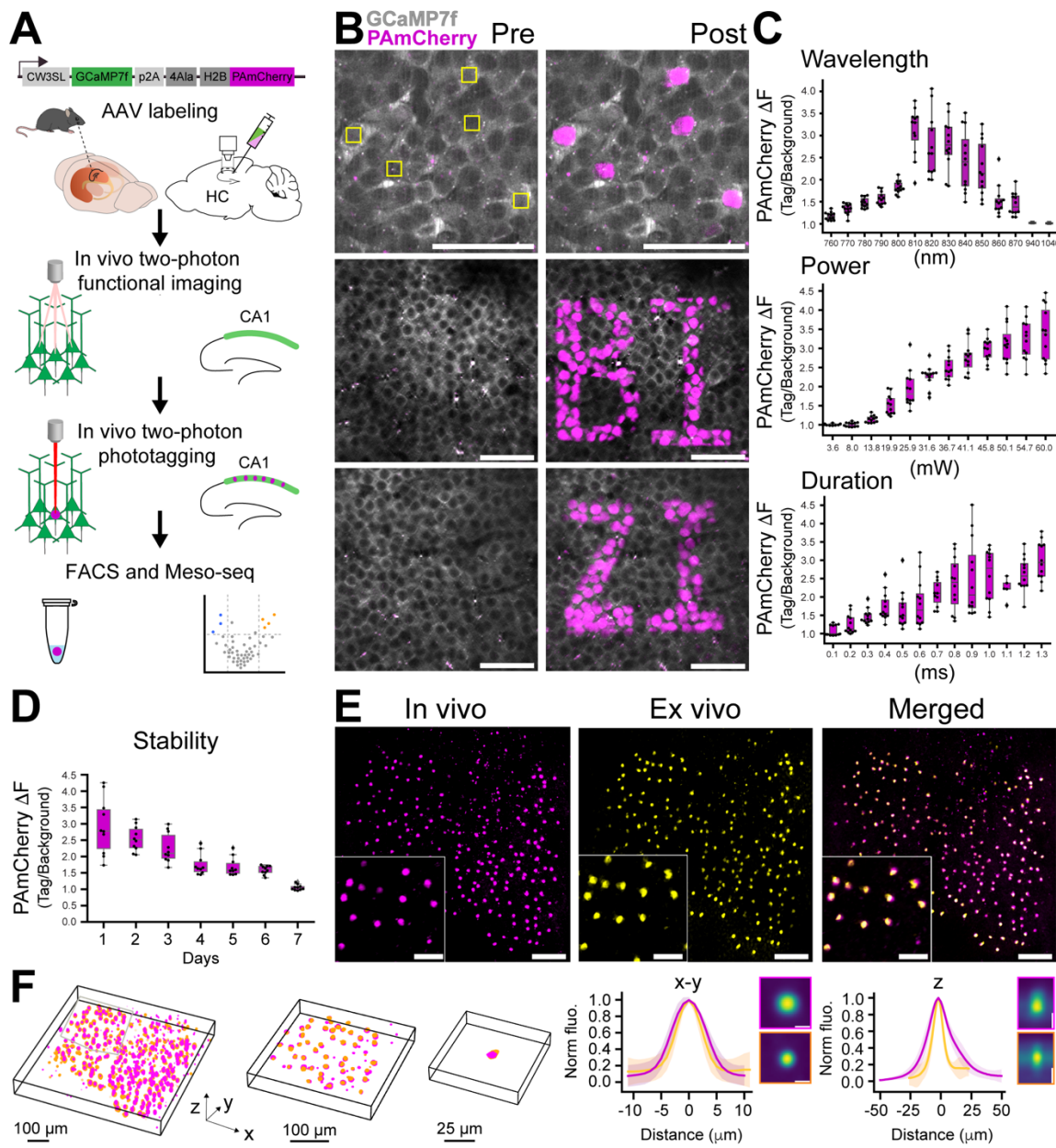
58 Results

60 *In vivo* two-photon phototagging with 2P-NucTag

61 A major challenge in combining *in vivo* functional recording with stable tagging in the same
62 neuron is the co-expression of an activity sensor and a photoactivatable tag with spectrally
63 separable fluorescent imaging and photoactivation. We overcame this challenge by generating a
64 bicistronic construct on a recombinant adeno-associated viral (rAAV) backbone that co-expresses
65 cytosolic GCaMP7f⁵¹ for 2P Ca^{2+} imaging and a nucleus-targeted photoactivatable red fluorescent
66 protein (H2B-PAmCherry) for 2P phototagging⁵⁰ via a promoter that is selective for cortical
67 glutamatergic neurons⁵² (2P-NucTag, Figure 1A). Upon injection of the 2P-NucTag rAAV into
68 the CA1 region of the mouse dorsal hippocampus to label CA1 PNs, we found that GCaMP7f is
69 properly expressed in the perinuclear space of the infected PNs (Figure 1B). Targeting the nuclei
70 of GCaMP-expressing neurons, we achieved rapid nuclear PAmCherry photoconversion using
71 810-nm excitation light on a three-dimensional acousto-optical deflector microscope (3D-
72 AOD)^{53,54} (Figure 1B; supplementary movie 1, see methods) and orthogonal GCaMP- Ca^{2+} activity
73 imaging with 940 nm excitation light (Figure S1A-B). Photoconverted PAmCherry red
74 fluorescence was detected at >1000 nm excitation (1040 or 1070 nm, see Methods) and was
75 localized to the targeted nuclei (Figure 1B, top). 2P-NucTag enabled the imprinting of arbitrary
76 tagging patterns into the CA1 pyramidal cell layer with 3D-AOD scanning, showing spatially
77 precise photoconversion of H2B-PAmCherry with single-nuclear and even sub-nuclear resolution
78 (Figure 1B, middle and bottom). We carried out a detailed characterization of wavelength, laser
79 power, and duration-dependence of PAmCherry photoactivation *in vivo* to identify the optimal
80 parameters for spatially precise photoactivation (Figure 1C). Based on our results, we opted for
81 810 nm excitation light with 37-42 mW laser power (measured after the objective), 1.3 ms/pixel
82 dwell time over 70 pixel x 70 pixel regions-of-interest (ROIs, with 0.1 $\mu\text{m}/\text{pixel}$ resolution). The
83 810-nm wavelength is spectrally separated from the GCaMP-based Ca^{2+} imaging wavelength at
84 940 nm, and these photoactivation wavelengths, laser power, and duration parameters yielded
85 robust increases in PAmCherry fluorescence of targeted nuclei (192-379% increase in PAmCherry
86 red fluorescence visualized using 1040 nm excitation: $n = 36$ cells, $295\% \pm 8\% \Delta F/F$, mean \pm
87 s.e.m.) after single scans while minimizing total scan time and power. We confirmed that
88 phototagged nuclei remained detectable over multiple days after photolabeling (Figure 1D). We
89 next photoactivated a subset of CA1 PNs in a large (700 x 700 μm) field of view (FOV), similar
90 to the FOV size used for *in vivo* 2P population imaging experiments in CA1 (Figure 1E, left). We
91 found clear photoactivation of individual target nuclei when visualized *in vivo*. We then confirmed
92 that *in vivo* photolabeling was preserved in *post hoc* histological slices (Figure 1E, middle), and

93 that phototagged cells can be reliably registered across *in vivo* z-stacks and *post hoc* confocal
94 images (Figures 1E, right, 1F, S1C-D, supplementary movie 2). In addition, we segmented the
95 nuclei from both the *in vivo* and *ex vivo* z-stacks to observe the average axial and lateral
96 fluorescence profiles of phototagged nuclei, demonstrating single-nucleus resolution (Figure 1F,
97 right).

98 To establish the compatibility of the 2P-NucTag construct with downstream cell sorting
99 and transcriptomic applications, we further prepared CA1 PN samples and subjected them to
100 FACS and Meso-seq (Figure S2). We chose to use our previously developed Meso-seq protocol
101 due to its advantage of providing a robust and cost-effective method for sequencing low numbers
102 of input nuclei. We collected 3 samples from AAV-transduced nuclei ('Injected, transduced'), 2
103 samples of nuclei that were not transduced but were isolated from the mice that received AAV
104 injections ('Injected, non-transduced'), and 2 negative control samples from mice that were not
105 injected with AAVs ('non-injected'). For each sample, 50-100 nuclei were collected and analyzed
106 in bulk via Meso-seq. Between these groups, we found that they have comparable sequencing
107 statistics in terms of total reads and percent of uniquely mapped reads (Figure S2A); notably, these
108 sequencing statistics were similar to those when we applied Meso-seq to AAV-infected visual
109 cortex samples in previous studies^{55,56}. Gene expression levels between groups were highly
110 correlated (Figure S2B-C) and reads of representative genes were similar between groups except
111 for the inhibitory neuron markers (Figure S2D). Thus, our results demonstrate that the previously
112 established Meso-seq protocol works well with low numbers of hippocampal PN nuclei as input,
113 and that the 2P-NucTag construct does not cause changes in transcriptional properties in AAV-
114 infected PNs. We also obtained *ex vivo* whole-cell patch-clamp intracellular recordings from
115 phototagged and control CA1 PNs (Figure S3A) in acute hippocampal slices: comparing H2B-
116 TAG (infected and photoactivated), H2B (infected), and control (non-infected) cells revealed no
117 differences in intrinsic properties (Figure S3B-G). Together, these results confirm the utility of 2P-
118 NucTag to analyze *ex vivo* the cellular properties of single CA1 PNs that were functionally
119 characterized and phototagged *in vivo* and demonstrate that the 2P-NucTag construct does not
120 affect the intrinsic physiological properties of these PNs. Thus, 2P-NucTag enables high-
121 throughput, indelible phototagging of neuronal nuclei *in vivo* that can also be identified via our
122 registration pipeline for *post hoc* analyses *ex vivo*. Phototagged nuclei further enable downstream
123 RNA-sequencing and *ex vivo* electrophysiology analyses.



124
125 **Figure 1. In vivo two-photon phototagging with 2P-NucTag.** (A) Schematics of the 2P-NucTag pipeline. Top:
126 bicistronic rAAV construct, injection to the hippocampus. Middle: *in vivo* two-photon (2P) GCaMP- Ca^{2+} population
127 imaging followed by 2P PAmCherry photoactivation, fluorescence-activated cell sorting (FACS), and mesoscale
128 sequencing (Meso-seq). (B) Top: representative *in vivo* time-averaged (6 frames average) 2P images of individual
129 cells before (Pre) and after (Post) *in vivo* two-photon PAmCherry photoactivation in the CA1 pyramidal layer of the
130 mouse dorsal hippocampus. Individual nuclei were photoactivated with 810-nm 2P laser chessboard scanning
131 region-of-interest (ROI, yellow boxes) over target nuclei (70 x 70 pixel for each ROI, 0.1 $\mu\text{m}/\text{px}$, 1.3 ms/px total pixel dwell
132 time, 6,370 ms total scan time per ROI. Laser power was 40 mW measured after the objective) with a 3-dimensional
133 acousto-optical deflector microscope (3D-AOD). Gray: GCaMP7f (940 nm excitation), magenta: PAmCherry, (1040
134 nm excitation). Scale bar: 50 μm . Middle and bottom: imprints of letters 'BI' and 'ZI' following patterned *in vivo*
135 two-photon photoactivation in the hippocampal CA1 pyramidal layer (scale bar, 50 μm). (C) Characterization of *in vivo*
136 2P photoactivation parameters for PAmCherry: duration, wavelength, laser power (measured after the objective) (n =
137 11-12 cells per condition). Relative change in PAmCherry red fluorescence (ΔF) is based on normalizing the tagged
138 nuclei fluorescence to the fluorescence of neighboring untagged nuclei measured with 1040 nm excitation. (D) *In vivo*
139 stability of the PAmCherry fluorescence signal over days after a single photoactivation scan (n = 8 cells). (E)

140 Representative time-averaged images from z-stacks of photoactivated nuclei *in vivo* (magenta: PAmCherry, scale bar:
141 100 μ m). Middle: *ex vivo post hoc* confocal z-stack image of the same field of view (FOV, magenta: PAmCherry).
142 Right: registered *in vivo* and *ex vivo* images following non-rigid image transformation (magenta: *in vivo*, yellow: *ex*
143 *vivo*, see methods). (F) Left: 3D overlay of tagged nuclei registered between *in vivo* (magenta) and *ex vivo* (yellow)
144 z-stacks with increasing lateral resolution (as in E). Gray box represents the segmented area for subsequent images.
145 Right: normalized lateral (x-y, left) and axial (z, right) fluorescence profiles (mean \pm s.e.m.) of tagged cells *in vivo*
146 (magenta, n = 1 mouse, 200 cells). Yellow: mean \pm s.e.m. of *ex vivo* confocal images (as in E and F, same mouse and
147 nuclei). Inset: (x-y) top: average *in vivo* maximum z-projection, bottom: average *ex vivo* maximum z projection; (z)
148 top: average *in vivo* lateral projection, bottom: average *ex vivo* lateral projection. Scale bar: 10 μ m. Boxplots show the
149 25th, 50th (median), and 75th quartile ranges, with the whiskers extending to 1.5 interquartile ranges below or above
150 the 25th or 75th quartiles, respectively. Outliers are defined as values extending beyond the whisker ranges.
151

152 **Phototagging of functionally identified PNs in the hippocampus *in vivo***

153 To demonstrate the utility of 2P-NucTag for on-demand labeling of functionally defined PNs, we
154 deployed 2P-NucTag to label hippocampal PNs located in the dorsal CA1, a region with well-
155 established spatial coding heterogeneity²⁸⁻³⁵. Only a subset of hippocampal PNs ('place cells')
156 exhibit reliable spatial tuning for a location ('place field') during exploration⁵⁷. Place cell identity
157 of PNs⁵⁸ is highly dynamic, with the majority of cells changing their spatial tuning properties over
158 the timescale of days³⁵⁻⁴⁰. While place cell properties of PNs were thought to be randomly
159 allocated onto seemingly homogeneous PNs⁵⁸, recent studies demonstrated that the genetic
160 expression profiles of CA1 PNs are also highly heterogeneous^{30,32,59}. These transcriptional
161 differences are present along all anatomical axes of the hippocampus²⁹, manifest at the protein
162 expression level, and are comprised of genes with known functions (e.g., transcription factors, cell
163 adhesion molecules, voltage-gated channels, neurotransmitter receptors, and auxiliary
164 subunits)^{29,60}. Gene expression differences thus could produce variability in the biophysical
165 properties and connectivity of PNs and may underlie the differences in stable spatial coding
166 properties of CA1 PN subpopulations. Thus, the spatial intermingling of place cells with active-
167 non-place and silent PNs⁶¹⁻⁶⁴ without apparent topographical organization in the densely packed
168 CA1 pyramidal layer^{35,64} allows us to test the utility of 2P-NucTag in selectively labeling PNs
169 occupying these distinct functional states.

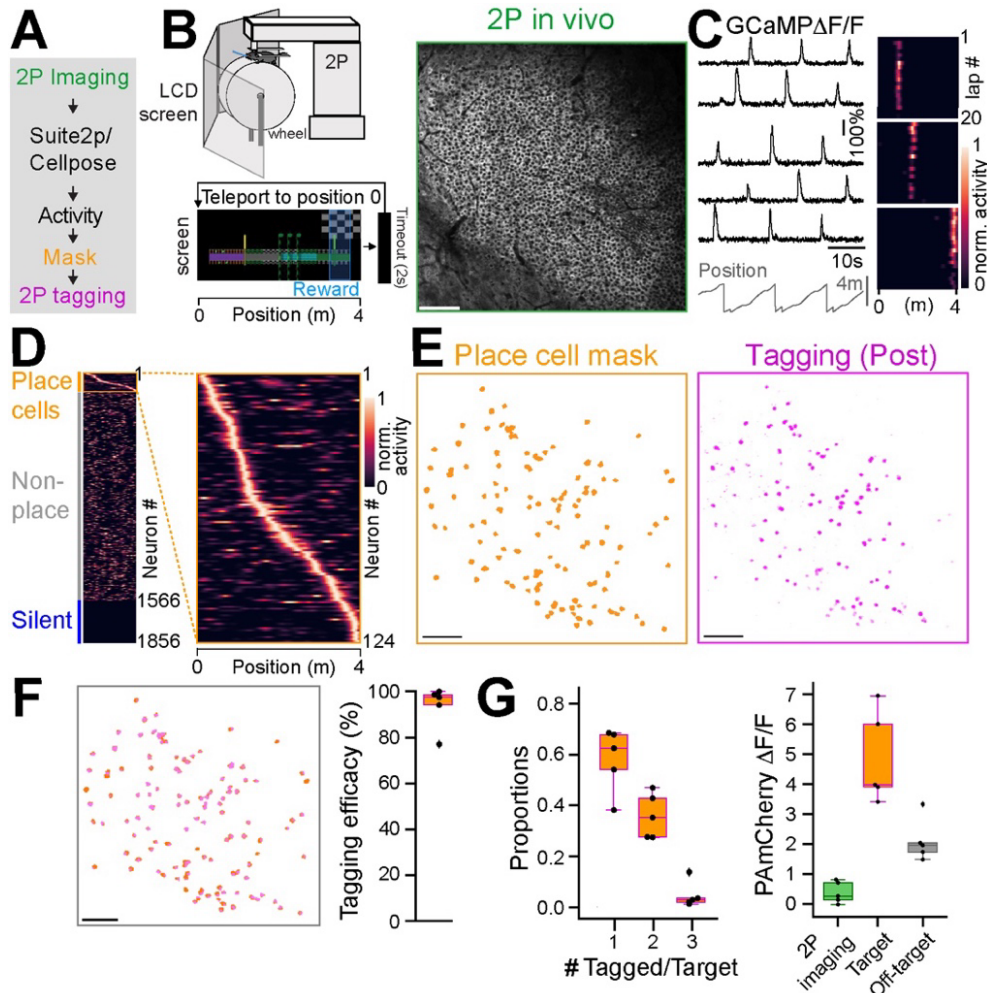
170 To selectively label CA1 PNs with distinct spatial coding properties, we trained mice in a
171 spatial navigation task for water rewards in a linear virtual reality environment⁶⁵⁻⁶⁷ and performed
172 *in vivo* 2P GCaMP- Ca²⁺ imaging of PNs (Figure 2A-B). We reliably detected GCaMP-Ca²⁺ signals
173 from individual PNs (Figures 2C, S1B). We analyzed the basic characteristics of GCaMP7f in the
174 bicistronic 2P-NucTag construct and confirmed that the basic properties of the indicator are similar
175 to those for a previously published single-construct version⁵¹ of GCaMP7f (Figure S1B). We
176 classified all PNs in the imaging FOV as place cells, active non-place cells, or silent cells (Figure
177 2D, see methods). Place cells were identified as described in our previous studies^{38,67-69} where
178 place fields were detected by identifying spatial tuning curves surpassing the 95th percentile of
179 shuffled tuning curve values, and silent cells were classified as cells with no deconvolved events
180 in the recording session. Following the functional identification of PNs, we generated spatial
181 masks of place cell locations in the FOV and used these masks to guide 2P phototagging of all
182 identified place cells in the imaging FOV with 3D-AOD (n = 5 mice, Figure 2E-F). In a separate
183 set of mice (n = 4 mice), we tagged a subset of CA1 PNs that exhibited no detectable activity
184 during the imaging session ('silent cells' see methods, Figure S4, Table 1), whereby we
185 photoactivated a similar number of silent cells as place cells in each mouse despite their higher
186 abundance in our recordings. We could reliably register photoactivated nuclei to the spatial masks
187 of functional profiles that we generated for cells of interest (Figures 2F, S4D-E, S5, see methods).

188 We quantified the number of place cell nuclei that we successfully photoactivated and compared
189 it to the number of spatial masks we generated for each animal. For silent cells, we performed a
190 similar calculation with number-matched silent cell nuclei. Across all animals, we phototagged
191 $93.3\% \pm 4.2\%$ ($n = 5$ mice) of all place cell masks and $53.6 \pm 6.6\%$ ($n = 4$ mice) of all silent cells
192 (Figure 2F).

193 To assess the accuracy of 2P photoactivation in the densely packed CA1 pyramidal layer,
194 we quantified the number of tagged nuclei for each targeted cell and found that photoactivation is
195 well restricted to the target cells' nuclei with limited off-target labeled nuclei, which had a smaller
196 increase in mCherry fluorescence (Figures 2G, S4F). After tagging, mCherry fluorescence
197 increased in targeted place cells ($487.7\% \pm 67\% \Delta F/F$, $n = 5$ mice) more than double compared to
198 the background and off-target fluorescence ($210.4\% \pm 32.1\% \Delta F/F$, $n = 5$ mice). Furthermore, 2P
199 GCaMP-Ca²⁺ imaging at 940 nm over the course of the imaging session (18-40 min, see Methods)
200 resulted in a minimal increase of mCherry red fluorescence ($37.4\% \pm 16.2\% \Delta F/F$, $n = 5$ mice,
201 Figure 2G, right, Figure S4F, 1070 nm excitation) and did not affect our ability to identify
202 phototagged neurons. Finally, mouse behavior and the quality of GCaMP recordings were
203 consistent between the two groups of mice (silent and place, Figure S4G-I).

204 To further confirm that photoactivation of the PAmCherry does not change the functional
205 response properties of neurons, we expressed the 2P-NucTag construct in the primary visual cortex
206 (V1) of adult mice and recorded visually evoked responses of neurons in this region before and
207 after photoactivation (Figure S6A). We found that the orientation tuning (including both
208 preference and selectivity) remained largely the same in visually responsive neurons following
209 photoactivation (Figure S6B-C), indicating that activation of the PAmCherry does not alter
210 neuronal response properties. These experiments were conducted in the visual cortex due to the
211 known stability of its tuning properties⁷⁰.

212 Thus, taken together, our experiments demonstrate that 2P-NucTag is suitable for on-
213 demand *in vivo* labeling of functionally defined neurons with high efficacy and accuracy.



214 **Figure 2. Selective phototagging of place cells in the hippocampus with 2P-NucTag.** (A) Pipeline for two-
215 phototagging of functionally identified hippocampal neurons during spatial navigation. (B) Left:
216 schematics of 2P imaging setup in virtual reality (VR). Head-fixed mice are trained to run for a water reward in a 4-
217 m long linear VR corridor projected onto LCD screens surrounding the animal. At the end of the corridor, mice are
218 teleported back to the start position after a 2-second delay. Right: example 2P field of view (FOV) of GcaMP in the
219 CA1 pyramidal layer. Scale bar: 100 μ m.(C) Left: Traces of relative GcaMP- Ca^{2+} fluorescence changes ($\Delta F/F$) from
220 five example CA1 place cells during VR spatial navigation. Right: heatmaps of normalized $\Delta F/F$ activity from three
221 example place cells over 20 laps during VR navigation. (D) Left: heatmap of all CA1PNs detected with
222 Suite2p/Cellpose in the FOV shown in B. Identified place cells are marked with an orange box. Right: Zoomed-in
223 heatmap of place cell tuning curves. (E) Left: spatial mask (orange) of identified place cells from D in the FOV.
224 Right: PAmCherry fluorescence (magenta) of tagged nuclei after 2P phototagging. Scale bar: 100 μ m. (F) Left:
225 overlay of spatial masks of identified CA1PNs and tagged nuclei for the FOVs in E. Scale bar: 100 μ m. Right:
226 tagging efficacy, defined as the fraction of successfully tagged place cell nuclei ($93.3\% \pm 4.2\%$, mean \pm s.e.m., $n = 5$
227 mice). (G) Left: Proportion of single, double, and triple-tagged nuclei following phototagging of a single place cell.
228 Right: relative change in PAmCherry red fluorescence (1070 nm excitation) for non-tagged cells in the FOV after 2P
229 imaging (green), after 2P phototagging of targeted place cell nuclei (orange) and off-target nuclei (gray, $n = 5$ mice).
230 Boxplots show the 25th, 50th (median), and 75th quartile ranges, with the whiskers extending to 1.5 interquartile
231 ranges below or above the 25th or 75th quartiles, respectively. Outliers are defined as values extending beyond the
232 whisker ranges.

233 **Transcriptional profiling of functionally identified CA1 PNs**

234 The ability to tag single cells *in vivo* enables a powerful new form of hypothesis generation and
235 testing by which functionally defined cells with known behavioral relevance can be isolated and
236 characterized. To demonstrate this, we sought to interrogate transcriptomic signatures of the
237 functional ‘place’ and ‘silent’ cell states of CA1 PN.

238 Following functional imaging and *in vivo* phototagging, brain tissue containing dorsal CA1
239 was collected at least 25 hours after functional imaging to eliminate the impact of immediate early
240 genes, and nuclei were dissociated and stained with a CoraLite 488-conjugated NeuN antibody
241 and DAPI to identify neuronal nuclei (see Methods). *In vivo* photoactivated nuclei were identified
242 by bright mCherry fluorescence (Figure 3A,B) and were isolated from the non-photolabeled
243 neuronal nuclei by fluorescent-activated cell sorting (FACS), enabling an estimated 18-67%
244 recovery of all photoactivated nuclei identified during *in vivo* imaging (Figure 3C). To validate
245 that the FACS events with bright mCherry fluorescence were indeed the desired nuclei, we also
246 performed sorting on samples derived from mice that were injected but not imaged; injected and
247 imaged; or injected, imaged, and phototagged (Figure S7): we set the gates for mCherry
248 fluorescence based on these samples and demonstrated that low mCherry fluorescence was
249 induced by the imaging laser (Figure S7B) since the phototagged nuclei exhibited clearly
250 identifiable higher mCherry fluorescence as compared to either of the other samples (Figure S7C).
251 We then collected these bright nuclei collected for downstream transcriptomic analyses. To
252 determine whether place cells and silent cells differed in their gene expression programs, RNA-
253 seq was performed on both populations of sorted nuclei by Meso-seq, an approach that enables
254 reliable identification of differentially expressed genes in ultra-low amounts for FACS-isolated
255 neuronal nuclei (i.e., tens of sorted nuclei per animal, Figure 3D)⁵⁵. After isolating the phototagged
256 nuclei, libraries were generated with the Meso-seq protocol and were sequenced at a depth of 40-
257 60 million reads per library (Figure S8A). Reads were aligned to the mm39 mouse genome
258 assembly with STAR, counted with HTSeq, and gene expression patterns were compared between
259 nuclei isolated from mice in which place cells were tagged (n = 5) and mice in which silent cells
260 were tagged (n = 4) via PyDESeq2.

261 In both populations, canonical CA1 PN marker genes (*Map2*, *Actb*, *Dlg4*, *Neurod6*) were
262 highly and non-differentially expressed, supporting the cellular precision of our tagging approach
263 (Figure 3E-F). However, 219 genes were identified as differentially expressed in a significant
264 manner between silent and place cells (Figure 3E, see Supplementary Table). In some cases,
265 specific genes were reliably identified in one group and absent from the other. For example, no
266 counts were measured for an inward rectifying potassium channel (*Kcnj12*) in place cell samples,
267 but the expression was present in all silent cell samples. Conversely, mRNA from two transcription
268 factors of the zinc finger protein family (*Zfp84*, *Zfp977*) and a protocadherin gene (*Pcdha8*) were
269 identified in every place cell sample and in none of the silent cell samples (Figure 3G). To ensure
270 that the observed differences did not arise from other sources of variation between our place and
271 silent cell samples, we performed several additional analyses, investigating potential contributions
272 from anatomical positioning, transcriptional responses to neural activity, cellular health, and sex.
273 Genes for which expression has been shown to vary along the dorsoventral and proximodistal axes
274 of CA1 were not differentially expressed in our place and silent-cell nuclei (Figure S8B)^{29,71},
275 indicating that any observed differences are unlikely to have originated from differences in
276 anatomical positioning during cell tagging. Immediate early gene levels (*Fos*, *Arc*, *Egr1*, *Npas4*)
277 did not differ (Figure 3F)⁷²⁻⁷⁴, suggesting that the ≥25 hours between the last behavior session and
278 tissue collection (see Methods) was sufficient time to eliminate the impact of immediate

279 transcriptional responses to neural activity. Apoptotic gene counts also did not differ between the
280 two groups (Figure S8), indicating that there was no significant difference in cell health between
281 the silent and place cells⁷⁵. Finally, to test for gross molecular differences between the cells in an
282 unbiased fashion, we performed gene set enrichment analysis on fifty hallmark gene sets from the
283 mouse molecular signatures database and found no significant differences between silent and place
284 cell samples (Figure 3H). Since the sex of mice used for both groups was not well balanced in this
285 study (Table 1), it is possible that gene expression differences originated from the mouse's sex
286 rather than the functional identity of the tagged cells. To explore this possibility, we compared
287 gene expression in randomly tagged (function-blind) CA1 PN nuclei from both male (n = 2) and
288 female (n = 2) mice. Although we found that known sex-specific genes⁷⁶ were differentially
289 expressed, none of the genes identified as enriched in either silent or place cells had significant
290 sex associations (Figure S9C,D). To assess if our differentially expressed genes-of-interest
291 signified upregulation or downregulation in place cells from the mean or, conversely,
292 downregulation or upregulation in silent cells, we compared gene expression in place cells and
293 silent cells to randomly tagged cells separately. We found that *Kcnj12* expression was enriched in
294 silent cells compared to random cells. *Zfp84* and *Zfp977* were significantly downregulated in silent
295 cells compared to random cells, while *Pcdha8* expression was significantly enriched in place cells
296 compared to random cells (Figure S9A,B).

297 Encouraged by our success in establishing 2P-NucTag for in-depth transcriptomic analyses
298 in 'place' and 'silent' cells, we next sought to further develop this approach for additional key
299 neurobiological applications. Specifically, we sought to test whether (1) the transcriptomic data
300 obtained with the 2P-NucTag can be validated and used for dissecting the molecular mechanisms
301 that determine functional properties of the phototagged neurons, and (2) 2P-NucTag can be used
302 for more nuanced cell populations and resolve genetic changes of the same functional cell group
303 at different timepoints.

304 For in-depth validation and functional analyses, we focused on *Kcnj12*, which our 2P-
305 NucTag based transcriptomic analyses identified as expressed in silent cells but not in place cells.
306 Since this gene encodes for an inward rectifying potassium channel Kir2.2⁷⁷⁻⁷⁹, we hypothesized
307 that its expression could reduce the intrinsic excitability of the neurons and make them more likely
308 to be silent. Thus, we first validated the differential expression of *Kcnj12* by performing
309 RNAscope Fluorescent in situ hybridization (FISH) in brain sections with tagged silent CA1 PNs
310 (Figure S10). Using a probe set for detecting *Kcnj12* (Figure S10A), we quantified the number of
311 *Kcnj12* puncta in tagged silent cells and a number-matched subset of randomly selected non-tagged
312 cells (n = 247 cells each, n = 3 mice). These analyses confirmed that tagged silent cells indeed
313 express more *Kcnj12* transcripts than non-tagged cells (Figure S10B). Similar RNAscope FISH
314 experiments for *Pcdha8* (Figure S10C) further confirmed the specificity of our 2P-NucTag-based
315 transcriptomic analyses since *Pcdha8* expression was enriched in tagged place cells as compared
316 to randomly selected non-tagged cells (Figure S10D, n = 321 cells in each subgroup, n = 3 mice).

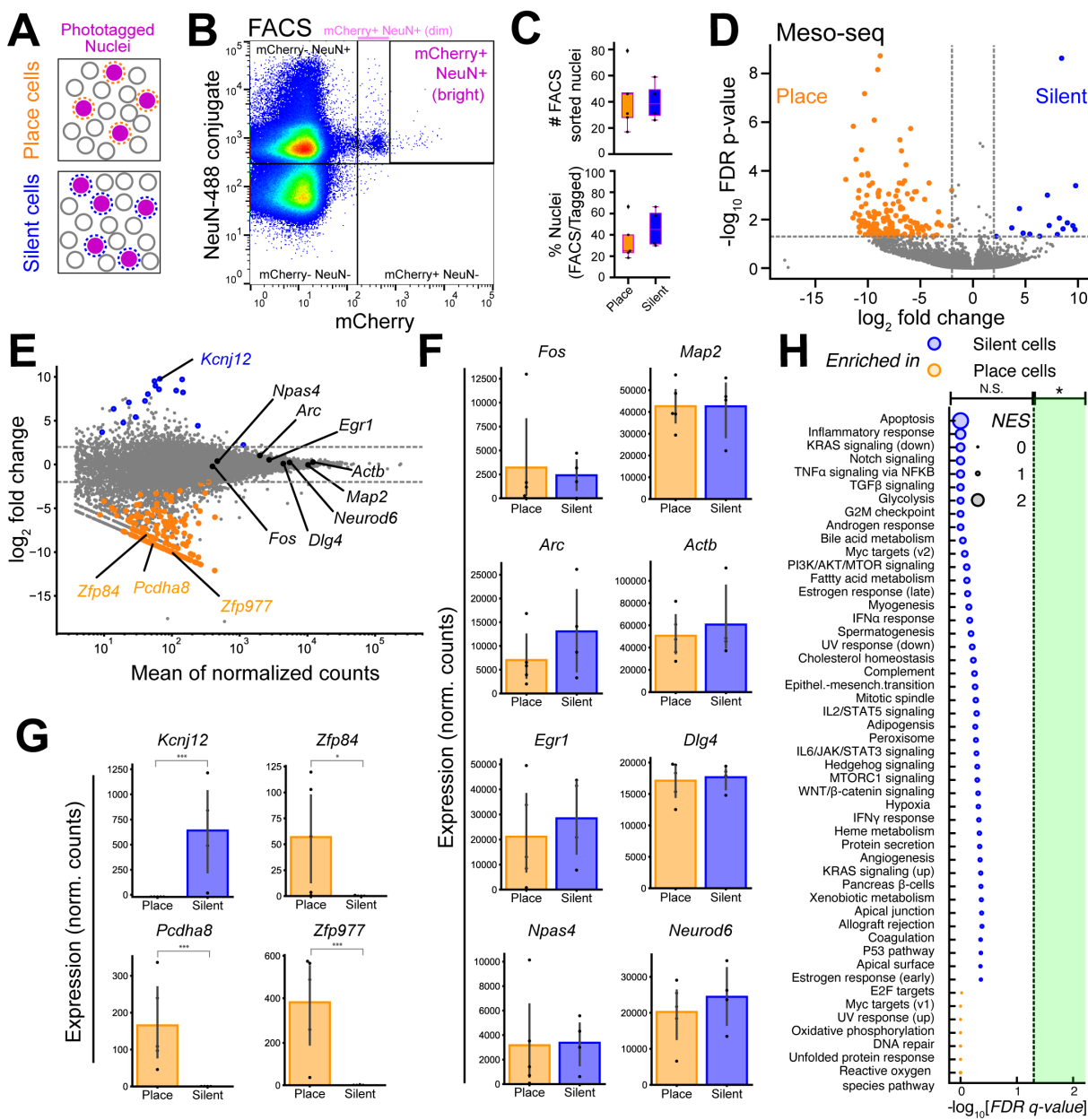
317 Next, we tested whether silent CA1 PNs differ in their intrinsic electrophysiological
318 properties. For this, we performed targeted whole-cell patch-clamp recordings from tagged silent
319 and nontagged cells *ex vivo* in acute hippocampal slices (Figure S11). Consistent with our
320 hypothesis, we found that silent cells had a hyperpolarized resting membrane potential as
321 compared to random non-tagged cells (Figure S11A). These experiments demonstrate the utility
322 of the 2P-NucTag approach not only for molecular and analyses in functionally defined neurons
323 but for connect *ex vivo* electrophysiological and cellular analyses of such *in vivo* labelled neurons.

324 Finally, to test whether the expression of Kir2.2 affects the likelihood of CA1 PNs to
325 become place cells, we designed an AAV vector for Cre-dependent expression of Kir2.2 along
326 with fluorescent protein mRuby3 (pAAV-hSyn-FLEX-Kir2.2_{WT}-T2A-mRuby3, Figure S12E); as
327 a negative control, we also designed a vector that drives expression of an inactive (non-conducting)
328 mutant of Kir2.2 (pAAV-hSyn-FLEX-Kir2.2_{Mut}-T2A-mRuby3, Figure S12E). We first co-injected
329 these vectors along with an AAV to drive the expression Cre-recombinase (pAAV-hSyn-Cre) into
330 the hippocampus of wild-type mice and assessed how ectopic expression of Kir2.2 affects the
331 excitability of infected neurons. Using targeted whole-cell patch clamping, we found reduced
332 excitability in cells expressing Kir2.2_{WT} (Figure S12A-D) as these cells had lower resting
333 membrane potentials, lower input resistance and lower firing rates across current steps when
334 compared to cells with the control virus (Figure S12B-D). We then sought to test the effect of
335 ectopic Kir2.2 expression on functional properties of CA1 PNs *in vivo* in behaving animals. We
336 used two sets of mice in which we co-injected either of the Kir2.2 vectors along with AAVs for
337 neuronal expression of GCaMP8s (pAAV-hSyn-GCaMP8s) and Cre-recombinase (pAAV-hSyn-
338 Cre) and trained mice in the same behavior paradigm as described in Figure 2. We found that the
339 cells expressing Kir2.2_{WT} are more silent than mRuby3-negative cells in the same field of view,
340 while these effects were not observed in cells with Kir2.2_{Mut} (Figure S12F). Comparisons of spike
341 rate and place cell percentage further indicated a silencing of activity and a lower proportion of
342 place cells in Kir2.2_{WT}-expressing CA1 PNs (Figure S12G-H). Therefore, expression of Kir2.2 in
343 CA1 PNs silences neurons, thereby affecting their *in vivo* function.

344 To further assess whether the 2P-NucTag approach can be used for molecular analyses in
345 cells with even more nuanced differences in *in vivo* activity and function, we transcriptomically
346 profiled place cells at different time points since a subset of these cells stabilizes their spatial
347 representations over time and thus might differ in gene expression from when place cells first
348 emerge. For this, we co-injected a version of 2P-NucTag AAV (pAAV-Ef1a-H2B-PAmCherry)
349 with an AAV for pan-neuronal expression of GCaMP8s (pAAV-hSyn-GCaMP8s) into the
350 hippocampal CA1 of two sets of mice. The mice were subsequently trained in a blank featureless
351 environment and then recorded in a feature-rich environment (Figure S13A). In one group, we
352 photo-tagged and collected place cells from day 0 of recording ('Day 0' cells), while in the other
353 group we continuously recorded the same FOV for 5 days, and photo-tagged and collected place
354 cells with at least 4 place fields across the 5 days of recording ('Recurring' cells, Figure S13B-C).
355 Transcriptomic analyses were done with Meso-seq as described before. Using this approach, we
356 identified 6 genes that were differently expressed (Figure S13D-F), including *Prkcd* and *Adamts1*,
357 two genes enriched in 'Recurring cells' which were previously found to play a role in memory and
358 synaptic connectivity^{80,81} and which therefore might control the synaptic wiring of neurons to
359 maintain long-term representation. Thus, we conclude that 2P-NucTag is useful for molecular
360 analyses in more nuanced cell types and cells with the same functional identity at different
361 timepoints.

362 Taken together, our results demonstrate that the 2P-NucTag approach allows for
363 identifying the molecular and cellular properties of neurons in the same brain region that differ
364 only by their activity patterns *in vivo* in behaving animals. Using this approach, we identify
365 previously unappreciated transcriptomic differences in "place" and "silent" cells in the
366 hippocampus of behaving mice and correlate these molecular profiles with the distinct
367 electrophysiological properties of these cells. We further revealed that these differentially
368 expressed genes affect the function of the respective groups of neurons by validating and
369 demonstrating the role of *Kcnj12* in the excitability of CA1 PNs and the functional consequences

370 when ectopically expressed. The 2P-NucTag approach has the advantage of revealing previously
371 unknown molecular profiles of PNs and works with other methods to dissect the contribution of
372 specific molecular processes.



373 **Figure 3. Post hoc transcriptional profiling of phototagged place and silent cells.** (A) Schematics of *in vivo*
374 photoactivated nuclei. ‘Place’ cell sample and ‘Silent’ cell samples from different mice were collected for FACS and
375 Meso-seq. (B) Representative FACS graph. Gating for mCherry was set after the first 5000 events of DAPI+ nuclei
376 to the border of the ‘dim’ mCherry+ population to separate out the sparse and high-intensity mCherry+ population.
377 Bright mCherry+ NeuN+ populations were collected as the photoactivated nuclei. (C) Top: number of FACS sorted
378 nuclei from ‘place’ and ‘silent’ samples ($n = 9, 17-79$ sorted nuclei, 40.3 ± 6.43 , mean \pm s.e.m.). Bottom: Proportion
379 of FACS sorted nuclei compared to the number of *in vivo* photoactivated nuclei ($n = 9, 18.45\%$ to 66.39% FACS
380 recovery, $39.94 \pm 6.30\%$, mean \pm s.e.m., ‘place’ mean = 34.63%, ‘place’ median = 25.0%; ‘silent’ mean = 46.59%,
381 silent median = 45.09%). (D) Volcano plot of Meso-seq differential expressed gene (DEG) analysis for ‘place’ and
382 ‘silent’ cells (significantly different genes are shown in orange and blue. Orange: enriched in place cells; blue: enriched
383 in silent cells). (E) Meso-seq MA plot depicting DeSeq2 normalized gene counts versus log₂ fold change of
384 silent/place samples. Genes that are significantly different are labeled in orange and blue (same as above). Genes
385 shown in panels F & G are highlighted and labeled in E. (F) Bar graph showing the normalized counts for genes that
386 are not differentially expressed (FDR adjusted q-value. * <0.05 , ** <0.001 , *** <0.001 , PyDeSeq2. Otherwise,
387 comparisons are not significant). (G) Bar graph showing the normalized counts for differentially expressed genes

388 (FDR adjusted p-value. * <0.05 , ** <0.001 , *** <0.001 , PyDeSeq2. Otherwise, comparisons are not significant). (H)
389 Gene ontology analysis performed on all differentially expressed genes. Vertical line: FDR-adjusted p value of 0.05.
390 NES = normalized enrichment score. Boxplots show the 25th, 50th (median), and 75th quartile ranges, with the whiskers
391 extending to 1.5 interquartile ranges below or above the 25th or 75th quartiles, respectively. Outliers are defined as
392 values extending beyond the whisker ranges.
393
394

395 Discussion

396 The comprehensive molecular-functional characterization of cortical circuits remains elusive due
397 to the limited toolkit for correlated *in vivo* functional recording techniques and *post hoc* molecular
398 analyses. Here, we introduced 2P-NucTag, a robust function-forward approach combining *in vivo*
399 imaging, on-demand single-nucleus tagging, and *post hoc* transcriptomics. This pipeline
400 seamlessly integrates 2P Ca²⁺ imaging in behaving mice, 2P phototagging of functionally
401 identified neuronal nuclei, FACS-isolation of the tagged nuclei, and subsequent analyses of
402 isolated nuclei with a mesoscale protocol for in-depth transcriptomics in ultra-sparse neuronal
403 populations.
404

405 We demonstrated the utility of 2P-NucTag by selectively labeling and analyzing
406 transcriptional profiles of two functionally orthogonal subpopulations of hippocampal PNs, ‘place’
407 cells and ‘silent’ cells, which remained inaccessible with existing techniques. Unexpectedly, our
408 experiments revealed a number of genes that are putatively differentially expressed between these
409 distinctly transient physiological cell states^{35–40}. The relatively low expression levels for some of
410 these genes indicate that further replicates may be necessary to confirm their differential
411 expression. Nevertheless, several of the identified genes generate new hypotheses about the
412 molecular mechanisms that underlie these two functional cell identities, which had been
413 molecularly indistinguishable otherwise. Specifically, the marked enrichment of an inward
414 rectifying potassium channel Kir2.2 (encoded by *Kcnj12*) in silent cells suggested that expression
415 of this gene might reduce the excitability of hippocampal pyramidal neurons to thereby lower the
416 activity of these cells *in vivo* and reduce their propensity to become place cells⁸². Indeed, our
417 experiments based on ectopic expression of *Kcnj12* are consistent with this idea, and thereby
418 implicate intrinsic excitability as a putative cellular and molecular mechanism that can influence
419 the activity and spatial coding properties of PNs in the hippocampus. Thus, our findings on *Kcnj12*
420 align with previous studies showing that intrinsic excitability is a major factor governing cell
421 recruitment to a memory trace^{83–86}. Future experiments will be needed to test the function of
422 specific genes that we have identified with our tagging technique, which could reveal a non-
423 random allocation of functional activity onto CA1 PNs during learning and experience. In
424 particular, future application of 2P-NucTag to selectively tag PNs with highly distinct and shared
425 coding properties, including place field propensity^{28,36,87,88}, recruitment to ‘replay’ and ‘preplay’
426 events^{89–92} and participation in functionally interconnected subnetworks⁶⁹ may uncover genetic
427 and developmental^{93–98} backbones of functional heterogeneity among PNs.

428 Our results showed low levels of unintended PAmCherry photoactivation during functional
429 imaging as well as limited off-target labeling. Although the activation level of these background
430 and off-target neurons is lower and the actual targeted cells’ photoactivation can be distinguished
431 through *in vivo* imaging, FACS, and *ex vivo* confocal imaging, this presents a complicating factor
432 e.g. when setting gating levels for FACS. Therefore, in this study, we sorted only the brightest
433 population of cells with high levels of mCherry fluorescence (Figures 3B, S7). Future optimization
434 of the phototagging vector and the 2P tagging parameters will help refine photoactivation
435 specificity. Nevertheless, our proof-of-principle implementation of 2P-NucTag to

436 transcriptomically characterize functionally heterogeneous hippocampal PNs that are spatially
437 intermixed in the densely packed pyramidal cell layer demonstrates that 2P-NucTag should be
438 readily applicable to neocortical tissue with lower cell density.

439 Beyond this first application to the mouse hippocampus, 2P-NucTag will have broad appeal
440 for correlated structural, molecular, and functional analysis of neural circuits. Our approach offers
441 the ability to bridge molecular, cellular-synaptic, and functional architecture in cortical circuits
442 and facilitates the identification of candidate genes that determine the distinct circuit functions of
443 neurons. Our results with ‘Recurring’ place cells further demonstrate that this pipeline should be
444 potent for uncovering molecular signatures of phenomenologically described neuronal subsets
445 with distinct feature selectivity, task-related activity, and longitudinal stability that are spatially
446 intermixed in cortical circuits^{21,23,25,99–103}.

447 Our approach can also be extended in multiple directions. Firstly, as 2P-NucTag is
448 compatible with *post hoc* histological analysis of imaged tissue, it can be combined with spatially
449 resolved transcriptomics^{17,18,104,105} following automated registration between *in vivo* and *post hoc*
450 images^{106,107}. Secondly, *ex vivo* electrophysiological recordings from tagged cells will allow for
451 detailed *ex vivo* physiological and anatomical characterization of the *in vivo* tagged cells^{9–12}.
452 Thirdly, while we opted to use Meso-seq for our transcriptomic analyses, our pipeline is
453 compatible with sc/snRNA-seq, given the single-cell resolution achieved through targeted
454 photoactivation. Fourthly, further optimization of phototagging with multi-color fluorophores may
455 enable simultaneous labeling of multiple functionally defined cell types in the same animal, while
456 cytosolic tags⁴⁸ can promote anatomical labeling of subcellular axonal or dendritic compartments
457 for downstream structural and connectivity analyses. Lastly, the on-demand nature of
458 photoactivation and its days-long stability following single photoactivation makes our pipeline a
459 valuable tool for precise analysis of transcriptional trajectories following cellular plasticity events
460 during, for example, behavioral learning^{53,74,108,109}.

461 In summary, our novel phototagging approach expands our understanding of the
462 fundamental relationship between the molecular and functional architecture of mammalian cortical
463 circuits and allows for the identification of candidate genes that determine the distinct circuit
464 functions of seemingly homogeneous populations of neurons. Beyond the proof-of-principle
465 implementation to hippocampal circuits, our approach provides a general framework and roadmap
466 for linking genes to cells across neural circuits and model organisms.

467 **Materials and Methods**

468 **Animals**

469 All animal care and experiment procedures were in accordance with the guidelines of the National
470 Institute of Health. Animal protocols were approved by the Columbia University Institutional
471 Animal Care and Use Committee and the Weizmann Institute of Science Institutional Animal Care
472 and Use Committee. Mice were group-housed under normal lighting conditions in a 12-hour
473 light/dark cycle. *Ad libitum* water was provided until the beginning of training for the spatial
474 navigation task.

475

476 **Plasmids and Viral Constructs**

477 pAAV-CW3SL-GCaMP7f-4Ala-H2B-PAmCherry was generated by standard cloning techniques.
478 GCaMP7f was PCR-amplified from Addgene plasmid #104492 with a 3' Primer that contained
479 sequences encoding four Alanine residues and the P2A sequence (both in frame with the coding
480 sequence of GCaMP7f). H2B-PAmCherry was amplified from Addgene plasmid #133419. The
481 PCR products were then subcloned by Gibson-assembly into Addgene plasmid #61463 after
482 removing EGFP from this plasmid by restriction with ClaI and EcoRI. The sequence of the cloned
483 plasmid was validated by Sanger sequencing and GCaMP7f + 4xAla, P2A and H2B-PAmCherry
484 were all found to be in frame. The plasmid was packaged into AAVDJ at a viral titer of 7.26E+15
485 essentially as described⁵⁵.

486 pAAV-hSyn-FLEX-Kir2.2_{WT}-T2A-mRuby3 and pAAV-hSyn-FLEX-Kir2.2_{Mut}-T2A-mRuby3
487 were generated at GenScript Inc. by synthesizing the respective inserts (Kir2.2_{WT}-T2A-mRuby3,
488 Kir2.2_{Mut}-T2A-mRuby3) and cloning them with standard cloning techniques into the viral
489 backbone AAV phSyn1(S)-FLEX-tdTomato-WPRE (Addgene plasmid # 51505). The gene
490 encoding the Kir2.2 channel was synthesized based on Genbank accession number
491 #NM_001267593 (i.e., isoform2 of mouse *Kcnj12*), and mRuby3 based on GenBank accession
492 number #KX987299.1. The plasmid was then packaged into AAVDJ at a viral titer of 1E+13. The
493 strategy of generating active WT channels and Mut control channels were similar to those used in
494 previous studies to generate active and inactive forms of Kir2.1^{56,110,111}.

495 pAAV-EF1a-H2B-PAmCherry was generated by standard cloning techniques. H2B-PAmCherry
496 was amplified from Addgene plasmid #133419 with the relevant sticky ends. The PCR product
497 was then subcloned using Enzymatic ligation into Addgene plasmid #203845 after removing
498 fDIO-mRuby3-2A-dCre from this plasmid by restriction with SalI and EcoRV. The sequence of
499 the cloned plasmid was validated by Sanger sequencing and H2B-PAmCherry were found to be in
500 frame. The plasmid was packaged into AAVDJ at a viral titer of 3.96E+13.

501

502 **Surgery**

503 All procedures were performed with mice under anesthesia using isoflurane (4% induction, 1.5%
504 maintenance in 95% oxygen). Mice's body temperature was maintained using a heating pad both
505 during and after the procedure. Surgeries were performed on a stereotaxic instrument (Kopf
506 Instruments). Before incision, mice were given subcutaneous meloxicam, as well as bupivacaine
507 at the incision site. Doses were calculated based on the animal's weight. An incision above the
508 skull was made to expose bregma and lambda for vertical alignment. Skull surfaces were cleaned
509 and scored to improve dental cement adhesion. For viral injection, a glass capillary loaded with
510 rAAV is attached to a Nanoject device (Drummond Scientific).

511

512 For hippocampal CA1 2P imaging mice except those described in Figure S12 and S13, viruses
513 were injected unilaterally in the left dorsal CA1 at 4 depths using the coordinates: -2.2 AP, -1.75
514 ML, and -1.2, -1.1, -1.0, -0.9 DV (relative to dura). At each depth, 75nl of AAVDJ-CW3SL-
515 GCaMP7f-4Ala-H2B-PAmCherry was injected. After injection, surgical sites were closed with
516 sutures. Three days after injection, the skull was exposed and a 3mm craniotomy was made
517 centered at the same coordinate of the injection site. Dura was removed, and the cortex was slowly
518 aspirated with continuous irrigation of cold 1X PBS until the fiber tract above the hippocampus
519 was visible. A 3-mm imaging cannula fitted with a 3mm glass coverslip was implanted over the
520 craniotomy site. Cannulas were secured by Vetbond. A custom titanium headpost for head-fixation
521 was secured first with C&B Metabond (Parkell) and then dental acrylic. At the end of each
522 procedure, the mice received a 1.0 ml saline injection subcutaneously and recovered in their home
523 cage with heating applied. Mice were monitored for 3 days after the procedure.
524 For mice used in Figure S12, 100nl of AAVDJ-hSyn-FLEX-Kir2.2_{WT/Mut}-T2A-mRuby3 + AAV9-
525 hSyn-GCaMP8s + AAV1-hSyn-cre were injected at 4 depths using the coordinates: -2.2 AP, -1.75
526 ML, and -1.2, -1.1, -1.0, -0.9 DV (relative to dura). All other surgery procedures are the same as
527 described above.
528 For mice used in Figure S13, 100nl of AAVDJ-Ef1a-H2B-PAmCherry + AAV9-hSyn-GCaMP8s
529 were injected at 4 depths using the coordinates: -2.2 AP, -1.75 ML, and -1.2, -1.1, -1.0, -0.9 DV
530 (relative to dura). All other surgery procedures are the same as described above.
531 For all visual cortex experimental mice, virus was injected unilaterally in the left visual cortex
532 using the coordinates: -2.7 AP, -2.5 ML, and -0.3 DV. 2-3 injections of 300 nl of virus were made
533 using a beveled glass micropipette to target layer 2/3 of the cortex at a rate of 65 nl/min using a
534 microsyringe pump (UMP3T-2, World Precision Instrument). A 4 mm craniotomy was made
535 above the visual cortex, and a coverglass and custom-made, 3D printed head post painted black to
536 allow for head fixation during imaging was glued to the skull using cyanoacrylate glue (Krazy
537 Glue). Following surgery, animals were administered with analgesic (0.1 mg/kg of buprenorphine
538 and 5 mg/kg of Carprofen). After initial recovery on a heating pad (RWD Life Science), mice were
539 returned to their homecage and monitored for post-op care.
540
541

542 **Behavior paradigm**

543 Mice were first water-deprived and habituated to handling and head fixation at least 7 days after
544 implant surgery. For behavior experiments in Figure 2 and Figure S13, mice were exposed to a 4-
545 m-long linear virtual reality (VR) corridor⁶⁵⁻⁶⁷ that stayed consistent in training and recording. For
546 behavior experiments in Figure S12, mice were first exposed to a 4-m VR corridor without features
547 ('blank' environment), and they were exposed to the feature-rich VR environment same as the
548 ones used in Figure 2 and Figure S13 on the first day of 2P functional imaging. At the end of the
549 environment, an inter-trial interval of 2 seconds of blank screen was included before the start of
550 the next lap. For the next 10-14 days, mice were trained to run through the virtual environment
551 and lick for a 5% sucrose reward. The rewards were first randomly distributed across the
552 environment, and the number of rewards was slowly reduced from 30 at the beginning of the
553 training to 2 when the mouse was deemed ready for recording. The final reward location was fixed
554 toward the end of the VR environment. Mice were trained to run at least 30-60 laps in the
555 environment. During behavioral imaging, mice were imagined during a single VR session (range:
556 18-40 min, 26 ± 3 min, n = 9 mice).
557

558 ***In vivo* two-photon imaging and data processing**

559 For 2P imaging of dorsal hippocampal CA1, 2P functional imaging was conducted using an 8-kHz
560 resonant scanner (Bruker) and a 16x near-infrared (NIR) water immersion objective (Nikon, 0.8
561 NA, 3.0-mm working distance). For population imaging in Figure 2 and Figure S12, a field of
562 view of 700 μ m x 700 μ m was acquired, and for population imaging in Figure S13, a field of view
563 of 420 μ m x 420 μ m was acquired. All imaging were done at 30 Hz, 512 x 512 pixels using a 940-
564 nm laser (Chameleon Ultra II, Coherent, 45-91 mW after the objective). Red (PAmCherry) and
565 green (GCaMP7f) channels were separated by an emission cube set (green, HQ525/70 m-2p; red,
566 HQ607/45 m-2p; 575dcxr, Chroma Technology), and fluorescence signals were collected with
567 GaAsP photomultiplier tube modules (7422P-40, Hamamatsu). Following the acquisition of two-
568 photon imaging data, Ca^{2+} imaging data was structured and aligned with behavior data using the
569 SIMA analysis package¹¹². CA1 ROIs were detected using the Suite2p (v0.14.2) package¹¹³. To
570 allow detection of all potential ROIs regardless of their activities during the recording, Suite2p
571 was run with Cellpose ('anatomical_only')¹¹⁴ for the ROI detection step. The pre-trained cyto2
572 model included in the published Cellpose package was used for ROI detection. When capturing
573 two-photon z-stack images of photoactivated PAmCherry nuclei, a fixed wavelength 1070-nm
574 laser (Fidelity-2W, Coherent) was used for excitation.

575 For 2P imaging of primary visual cortex, a two-photon microscope equipped with a 12 kHz
576 resonant-galvo scanhead (Bergamo microscope, ThorLabs) was used with a Ti:Sapphire laser
577 (MaiTai DeepSee, Spectra Physics). Imaging data was concatenated, registered, ROIs were drawn
578 and fluorescence was extracted using Suite2p. Following this, all recordings were analyzed using
579 custom software written in house in MATLAB (MathWorks). F signals were neuropil corrected
580 and aligned to timing of visual stimulation using frame time signals collected in Clampex
581 (Molecular Devices) during recording sessions and averaged across repetitions. Field of views
582 (FOVs) were mapped in order to determine the location of V1 and best imaging area for recordings
583 per animal. Receptive fields were mapped by presenting patches of drifting sinusoidal gratings
584 spaced on a 3 by 4 grid of the monitor. Stimuli were presented for 1 s at 0, 100% contrast and 0.04
585 cpd with an interstimulus interval of 4 s. FOVs were selected based on receptive field mapping
586 and percentage of visually responsive neurons in the area.

587

588 **Visual stimulation before and after phototagging**

589 Visual stimuli were generated using the MATLAB Psychophysics toolbox
590 (<http://psychtoolbox.org/>) and presented on a gamma-corrected LCD screen. The screen was
591 positioned 20 cm from the contralateral eye of the recorded hemisphere. Stimuli were presented
592 for 1 s with an interstimulus interval of 4 s during which a gray screen of mean luminance was
593 presented. Visual stimuli consisted of full-field sinusoidal drifting bar gratings with a temporal
594 frequency of 2 Hz. Varying directions (equal spacing of 30) were presented in a pseudorandom
595 order with 24-25 repetitions per stimulus type.

596

597 ***In vivo* two-photon phototagging**

598 Photoactivation was conducted using a three-dimensional random-access acousto-optical (3D-
599 AOD) microscope (3D Atlas, Femtonics)^{19,54}. Mice were head-fixed and anesthetized with
600 isoflurane to minimize motion and increase the spatial precision of phototagging. The same 16x
601 NIR water immersion objective was used to find the same field of view as in the functional
602 recordings. Photoactivation was performed at 810-nm (Chameleon Ultra II, Coherent). Two-
603 photon images of the mCherry red fluorescence were taken before and after photoactivation using

604 a 1040-nm excitation laser (Alcor 1040-5W, Spark Lasers). Red (mCherry) and green (GCaMP7f)
605 channels were separated by an emission cube set (green, HQ520/60 m-2p; red, HQ650/160 m-2p;
606 565dcxr, Chroma Technology), and fluorescence signals were collected with GaAsP
607 photomultiplier tube modules (7422P-40, Hamamatsu). Two-photon images of the mCherry red
608 fluorescence were taken before and after photoactivation using a 1040-nm excitation laser (Alcor
609 1040-5W, Spark Lasers). For photoactivation, a 7 x 7 μm , 0.1 μm /pixel scanning pattern was
610 placed on the cell to be photoactivated. Each pixel was activated for a total dwell time of 1.3 ms
611 with a laser power of 40 mW. This gave the total scanning time of each cell at 6,370 ms. Following
612 photoactivation, a z-stack was taken for each mouse to assess the photoactivation efficacy.
613 For phototagging of ‘place cells’ and ‘silent cells’, photoactivation experiments were conducted a
614 day after functional recording sessions. For phototagging of ‘Day 0 cells’ and ‘Recurring cells’,
615 photoactivation experiments were conducted the same day as functional recording sessions. The
616 imaging field of view of 700 μm x 700 μm was matched between the 3D-AOD microscope and
617 the time-averaged GCaMP image from functional recording. After confirming the same field of
618 view as functional imaging, the viewport was zoomed in to a dimension of 250 x 250 μm for more
619 effective identification of targeted cells according to the generated spatial masks. Following
620 photoactivation of all cells, a z-stack image was taken for each mouse to confirm the tagging
621 accuracy. Mice were given *ad libitum* water after functional imaging for at least 12 hours before
622 photoactivation. During the session, mice were monitored every 10 min for breathing rate and
623 reflexes. Heating and eye ointment were applied. Following the photoactivation, mice were
624 returned to the home cage to recover with a heating pad.
625 For phototagging of neurons in the primary visual cortex, a 405 nm LED light was used to
626 illuminate the field of view for 30 seconds to achieve photoactivation of most of the infected
627 neurons, and photoactivation of neurons were confirmed by recording in the red channel using a
628 1040 nm laser before and after photoactivation.

629
630 **Tissue dissociation and preparation of nuclei for FACS**
631 For all animals used in this manuscript, tissue collection was performed at the same time of the
632 day (5 pm) and at least one hour after the photoactivation. Mice were euthanized using CO₂. The
633 headpost and metal cannulas were removed. Dorsal CA1 of the hippocampus was collected by first
634 using a 3-mm biopsy punch to cut a circular section of tissue the same size as the craniotomy. A
635 microspatula was used to remove the shallow section of tissue that contained dorsal CA1. The
636 tissue was placed in a 1.5 ml RNase-free Eppendorf tube and snap-frozen in liquid nitrogen.
637 Tissues were stored at -80 °C until the start of the nuclei isolation.

638 Nuclei were prepared for FACS sorting essentially as previously described (46). In short, to isolate
639 the nuclei, each collected tissue was transferred to a dounce tissue homogenizer (DWK Life
640 Sciences) with 1ml of homogenization buffer (10 mM Tris Buffer, 250mM Sucrose, 25 mM KCl,
641 5mM MgCl₂, 0.1mM DTT, 0.1% Triton X-100, 1X Protease Inhibitor Cocktail, and 40U/ μl
642 RNAsin Plus RNase Inhibitor in nuclease-free water). Loose and tight pestles were used to break
643 apart the tissue 10 times each. Following the homogenization, 1 ml of homogenization buffer was
644 added to each dounce, and the homogenate was pipetted up and down to further break apart tissue
645 before being passed through a 30 μm cell strainer (Miltenyi Biotec) and collected in a 15 ml conical
646 tube.

647 The homogenate was centrifuged at 4 °C, 700g for 8 min. The supernatants were then removed
648 from the visible nuclei pellet. The nuclei pellet was resuspended with 800 μl of blocking buffer
649 (1X PBS, 1% BSA, and 40 U/ μl RNasin Plus RNase Inhibitor in nuclease-free water). The

650 resuspension was incubated on ice for 15 min and transferred to a 1.5 ml tube. 2 μ l of CoraLite
651 Plus 488-conjugated NeuN Monoclonal antibody (Proteintech) was added to the resuspension, and
652 incubated on an orbital rotator at 4 °C for 30 min. After incubation, nuclei were centrifuged at 4
653 °C, 700 g for 8 min. The supernatant was removed, and the nuclei pellet was resuspended with
654 1000 μ l of blocking buffer. DAPI was added to the suspension at a final concentration of 0.001
655 mg/ml, and the samples were passed through a 40- μ m Flowmi Cell Strainer (Bel-Art). All samples
656 were kept on ice until the start of FACS.

657

658 **Fluorescence-activated cell sorting (FACS)**

659 The sorting was performed at the Zuckerman Institute Flow Cytometry Core using a MoFlo Astrios
660 Cell Sorter (Beckman Coulter). Event rates were kept between 5000-10000 events per second. The
661 cell sorter uses a linear array of lasers ordered as 640 nm, 488 nm, 561 nm, 532 nm, 405 nm and
662 355 nm from top to bottom. For experiments described in this manuscript, 488 nm, 561 nm and
663 405 nm lasers were used to detect the fluorescence of NeuN, mCherry and DAPI respectively. A
664 gating control sample was used to set the gates for DAPI, NeuN and mCherry. Dissociated nuclei
665 were passed through the cell sorter to collect those with high mCherry signals. Bright and Dim
666 mCherry gates were determined after the first 5000 events of DAPI-positive nuclei. Gating was
667 set to collect only the sparse and bright population that showed a high mCherry signal, and these
668 events were collected as the photoactivated nuclei ('Bright' mCherry). Nuclei were collected into
669 SMART-Seq CDS sorting buffer that contains 1X lysis buffer, SMART-Seq Oligo-dT and RNase
670 inhibitor. All sorted samples were kept on dry ice as recommended by the SMART-Seq protocol
671 until the start of first-strand synthesis. To increase the likelihood of collecting nuclei in this ultra-
672 sparse population, aborted events for 'Bright' mCherry and all events for other positive mCherry
673 were collected into the blocking buffer (200 ml). This suspension was passed through the sorter
674 again with the same fluorescence gating following the completion of the first sorting to capture
675 the bright nuclei.

676

677 **Meso-seq**

678 We followed the previously published Meso-seq protocol⁵⁵ with minor modifications. Sorted
679 nuclei were collected in a lysis buffer following the SMART-Seq mRNA LP protocol. Reverse
680 transcription for cDNA was followed by cDNA amplification using 17-18 PCR cycles. Purified
681 cDNA was prepared for sequencing the library using the SMART-seq Library Preparation Kit.
682 Libraries were amplified using 14 PCR cycles. The concentration of the final library was
683 determined using a Qubit3.0 Fluorometer (Invitrogen), and the average DNA fragment size was
684 determined using a Bioanalyzer (Agilent). Sequencing was performed on a NextSeq 2000
685 sequencer with P2-100 reagents (Illumina). Libraries were diluted and pooled according to the
686 recommendation of the sequencing kit.

687

688 ***Ex vivo* electrophysiology in acute hippocampus slices**

689 Mice were transcardially perfused with ice-cold sucrose dissection media (26 mM NaHCO₃, 1.25
690 mM NaH₂PO₄, 2.5 mM KCl, 10 mM MgSO₄, 11 mM glucose, 0.5 mM CaCl₂, 234 mM sucrose;
691 340 mOsm). Brains were then dissected and sliced, while being kept in ice-cold sucrose dissection
692 media, into coronal sections (300 μ m thick) containing the hippocampal CA1 using a Leica
693 VT1200S vibratome. Slices were incubated in high osmotic concentrated artificial cerebrospinal
694 fluid (aCSF) (28.08 mM NaHCO₃, 1.35 mM NaH₂PO₄, 132.84 mM NaCl, 3.24 mM KCl, 1.08
695 mM MgCl₂, 11.88 mM glucose, 2.16 mM CaCl₂; 320 mOsm) at 32 °C for 30 minutes immediately

696 after slicing. Then, slices were incubated in normal osmotic concentrated artificial cerebrospinal
697 fluid (26 mM NaHCO₃, 1.25 mM NaH₂PO₄, 123 mM NaCl, 3 mM KCl, 1 mM MgCl₂, 11 mM
698 glucose, 2 mM CaCl₂; 300 mOsm) at 32°C for 30 minutes and subsequently at room temperature.
699 All solutions were saturated with 95%-O₂/5%-CO₂, and slices were used within 6 hours of
700 preparation. Whole-cell patch-clamp recordings were performed in aCSF at 32°C from neurons in
701 the hippocampus. Recording pipettes were pulled from borosilicate glass capillary tubing with
702 filaments (OD 1.50 mm, ID 0.86 mm, length 10 cm) using a P-700 micropipette puller (Sutter
703 Instruments) and yielded tips of 3–5 MΩ resistance. Recordings were sampled at 20 kHz and
704 filtered at 3 kHz. Data were acquired via Clampex10 using a Multiclamp 700B amplifier and
705 digitized with an Axon Digidata 1550B data acquisition board (Axon Instruments). Tagged
706 neurons were identified based on mCherry nuclear fluorescence using a pE-300 white MB LED
707 light (CoolLED) with GYR (525–660nm) spectrum, combined with an Olympus Cy5 Filter Cube
708 Set (ex. 604-644nm; em. 672-712nm).

709 To ensure that the recorded cells were indeed phototagged neurons, Alexa 594 Hydrazide (10uM)
710 was added to the internal solution to allow co-localization of the fluorescence of the tagged neuron
711 to the one that was patched using confocal imaging in PFA(4%)-fixed slices.

712 For measuring the intrinsic properties, the following internal solution was used: 135 mM k-
713 gluconate, 4mM KCl, 10mM HEPES, 10mM Pcreatine, 4mM Mg-ATP, 4mM GTP-Na and 2mM
714 Na₂-ATP. Intrinsic properties were calculated by giving 1.2s long current steps (20pA).

715

716 **Tissue collection and processing for *in situ* hybridization**

717 Mice were anesthetized with isoflurane and transcardially perfused with 20 mL of ice-cold 0.01M
718 phosphate base saline (PBS, Sigma) followed by 20 mL ice-cold 4% paraformaldehyde (PFA,
719 Electron Microscopy Sciences) in PBS. Brains were post-fixed in 4% PFA for 24 hours and then
720 saturated with a 10%, 20%, and 30% sucrose solution sequentially over 48 hours until they sunk
721 to the bottom of each successive solution. 30% Sucrose-saturated brains were then embedded in
722 OCT (Optimal Cutting Temperature Compound, Sakura, cat#4583), frozen, stored overnight at -
723 80 °C, and sliced transversely at 20 μm thickness with a cryostat. Sections were stored at -80 °C
724 on slides and used for RNAscope *in situ* hybridization.

725

726 **RNAscope Fluorescent In Situ Hybridization (FISH)**

727 20 μm fixed frozen sections of the frozen tissue block were taken and the RNAscope™ Multiplex
728 Fluorescent Reagent Kit v2 – User Manual was followed (cat#: 323100). The *Kcnj12* targeting
729 probe was designed for *Mus musculus* and generated by Advanced Cell Diagnostics Inc (C3: Cat
730 No. 525171, Entrez Gene ID: 16515, GenBank Accession #: NM_010603.6), and same for the
731 *Pcdha8* probe (C1; Cat No. 841011, Entrez Gene ID: 353235, GenBank Accession #:
732 NM_201243.1). Slides were sequentially dehydrated using ethanol solutions of increasing
733 concentrations (50%, 70% and 100%) for 5 min each at RT. 5-8 drops of H₂O₂ were added to each
734 sample, followed by a 10 min incubation at RT. After rinsing with distilled water, antigen retrieval
735 was performed for 5 min at 99°C (shorten from the manufacturer's recommendation to preserve
736 PAmCherry fluorescence while maintaining RNAscope signal). To digest sections, RNAscope
737 Protease III was applied to the sections for 30 min at 40°C. The probes were hybridized for 2 h at
738 40°C and amplified with AMP1 (30 min), AMP2 (30 min), AMP3 (15 min); each was incubated
739 at 40°C. The probe was fluorescently tagged with 1:2000 TSA Vivid Fluorophore 650 (PN
740 323273). Slides were counterstained with DAPI for a nuclear stain to identify viable cells and

741 mounted in ProLong Gold Antifade Mountant. 20 μ m sections were imaged in 3 μ m z-steps using
742 an inverted confocal microscope with 20x air objective (A1 HD25, Nikon Instruments Inc.).
743

744 **Data analysis**

745 **Quantification and Statistical Analysis**

746 All statistical details for comparisons are described in the text. No statistical methods were used
747 to determine sample sizes. Boxplots show the 25th, 50th (median), and 75th quartile ranges with the
748 whiskers extending to 1.5 interquartile ranges below or above the 25th or 75th quartiles,
749 respectively. Outliers are defined as values extending beyond the whisker ranges. For comparisons
750 between two populations with non-normal distributions, the Mann-Whitney U test was used. For
751 comparisons between gene expression datasets, the Wald test followed by multiple corrections via
752 the Benjamini and Hochberg method was used as described in PyDESeq2¹¹⁵.
753

754 **Event detection**

755 Fluorescence GCaMP traces were deconvolved using OASIS for fast nonnegative
756 deconvolution¹¹⁶. As in ref.¹¹⁷, these putative spike events were filtered at 3 median absolute
757 deviations (MAD) above the raw trace, using a predetermined signal decay constant of 400 ms.
758 The binarized signal was used to qualify whether a neuron was active at the respective frame. In
759 our analysis, we do not claim to uncover true spiking events in these neurons but use deconvolution
760 for denoising and diminishing Ca^{2+} autocorrelation.
761

762 **Spatial tuning curves**

763 The virtual environment was divided into 100 evenly spaced bins (4 cm), which were then utilized
764 to bin a histogram of each cell's neuronal activity. Neuronal activity was filtered to include activity
765 from when the animal was running above 3 cm/s and to exclude activity during the 2-sec
766 teleportation at the end of the 4-m track. The spatial tuning curves were normalized for the animal's
767 occupancy and then smoothed with a Gaussian kernel ($\sigma = 12$ cm) to obtain a smoothed activity
768 estimate.
769

770 **Place cell detection**

771 Place fields were detected by identifying locations in the virtual environment where a neuron was
772 more active than expected by chance. We circularly shifted each neuron's deconvolved spike trace
773 and recomputed the smoothed, trial-averaged spatial tuning curve of the shifted trace to generate
774 a shuffled null tuning curve per cell. We repeated this procedure 1000 times in order to calculate
775 the 95th percentile of null tuning values at every spatial bin to generate a threshold for a $p < 0.05$
776 significance curve. Spatial tuning curves that surpassed the null threshold were marked as
777 candidate place fields, and the place field width was calculated as the total bins where the tuning
778 curve exceeded the shuffled null tuning curve. To restrict our analysis to neurons with specific
779 firing fields, we additionally required that place fields have a width greater than 8 cm and less than
780 one-third of the virtual environment (1.3 m). To ensure that the place field activity was stable, we
781 also required that all place cells had activity for at least 20 laps.
782

783 If the binarized signal trace for a cell did not have any detected events via OASIS deconvolution,
784 the cell was classified as silent.
785

786 For experiments described in Figure S12, five consecutive days of recording were first
787 concatenated as one image sequence and Suite2P was used for motion correction and ROI-
788 detection. They were then separated into recording for each day for analysis. Place fields detection
789

787 were performed for each cell for each recording days, and same ROI number were used across
788 days. Cells with place field for at least 4 out of 5 days were classified as ‘Recurring’ cells. ‘Day
789 0’ cells were place cells with place fields on the first recording day, done in a separate set of
790 animals.

791

792 **PAmCherry fluorescence quantification**

793 (Figure 1C,D)

794 Red PAmCherry fluorescence was calculated as the tagged nuclei fluorescence versus the
795 background fluorescence of nearby untagged nuclei for the image taken post-tagging. This was
796 intentional to control for periodic two-photon imaging at 940 nm that may cause an increase in
797 fluorescence for every cell in the FOV.

798

799 **Fluorescence intensity distribution analysis**

800 (Figure 1F, right)

801 Red PAmCherry tagged nuclei were segmented using Cellpose with manual curation performed
802 within the Cellpose GUI for the max axial projections of the *ex vivo* z-stack (excitation: 568 nm
803 nm) and *in vivo* z-stack (1070 nm) to generate masks. The masks were used to segment the 3-D
804 volumes of each cell and the respective fluorescence profiles were normalized and aligned based
805 on the peak value. The average and standard error were computed based on the aligned
806 fluorescence profiles of the cells from the respective *in vivo* and *ex vivo* volumes.

807

808 **Two-photon background excitation fluorescence quantification**

809 [Figure 2G(2P imaging), Figure S4F (2P imaging)]

810 Changes in PAmCherry red fluorescence due to two-photon fluorescence excitation at 940 nm
811 from functional recordings were examined. By taking the average fluorescence of the pre-imaging
812 red channel image and post-imaging red channel image detected at 1070 nm, $\Delta F/F$ was computed
813 using the change in fluorescence between the average post-imaging red image and pre-imaging
814 red image divided by the pre-imaging red image average $[(\text{post} - \text{pre}) / \text{pre}]$.

815

816 **Tagged and Off-target Fluorescence Change Quantification**

817 [Figure 1G (target, off-target), Figure S4F (target, off-target)]

818 Tagged nuclei were segmented using Cellpose with manual curation performed within the
819 Cellpose GUI for the max axial projection of the *in vivo*-stacks from each mouse to generate masks.
820 These masks were used to segment a 3D volume for each nucleus that was targeted across all mice.
821 The number of off-target nuclei was manually quantified laterally and axially per targeted nuclei.
822 Masks for off-target nuclei were hand-drawn on the max axial projection to exclude the targeted
823 nuclei and were at most 2 nuclei bodies away. Experimental background fluorescence masks were
824 drawn on the surrounding areas with successfully tagged nuclei and excluded all targeted and off-
825 target nuclei.

826 The fluorescence values for all tagged and off-target nuclei were percentile-filtered to exclude the
827 lower 10% of fluorescence values to account for vignetting effects and mask inhomogeneities over
828 the max axial projection. Background fluorescence levels were selected in the areas of field of
829 view without tagged nuclei. The percentile filtered fluorescence values for tagged and off-target
830 nuclei were averaged, and the $\Delta F/F$ was computed by taking the difference between the average
831 tagged or off-target fluorescence value and the average background fluorescence and then
832 normalizing by the average background fluorescence [tagged: (tagged – background)/background;

833 off-target: (off-target – background)/ background]. Note this background value is distinct from the
834 one described in the two-photon background excitation fluorescence quantification.

835

836 **GCaMP quantifications**

837 [Figure S1AB, Figure S4I]

838 Frequency: The total number of deconvolved events by OASIS was normalized by the total
839 duration of the recording.

840 For each cell, the average transient was segmented within a 15-second time window and computed
841 by averaging along aligned deconvolved spike times. If multiple detected events were within 50
842 frames, the events were treated as a single transient. A cell was only used if there were at least 3
843 detected transients within the total trace to exclude cells without obvious GCaMP-Ca²⁺ dynamics.

844 For each average transient, we computed the median value based on 5 seconds pre peak transient
845 and the range 5-10 seconds after the peak transient (given that the average transient took
846 significantly less than 5 seconds to resolve) to act as the baseline.

847 Amplitude: The difference between the max value of the average transient and the baseline value
848 was computed

849 Half-Rise Time: The time between the half-max value prior to the max and the max value of each
850 transient was computed. We excluded cells where the average half-max value was not observed
851 prior to the transient and performed 99th percentile filtering to remove extreme outliers. Due to
852 sampling rate limitations, we cannot comment on the true half-rise time, so these are
853 approximations.

854 Half-Decay Time: We computed the time between the max and the half-max value following the
855 transient peak. To remove extreme outliers, we performed 99th percentile filtering.

856

857 **Visually evoked neural activity**

858 [Fig. S6]

859 Visually evoked responses were calculated as the mean $\Delta F/F$ during visual stimulus presentation:
860 $\Delta F/F = (F - F_0)/F_0$

861 Where F_0 was calculated as the mean fluorescence during the 1 second preceding the visual
862 stimulus. To determine if a cell was visually responsive, a one-way non-parametric ANOVA
863 (Kruskall-Wallis) was computed comparing the evoked responses to baseline fluorescence. An
864 additional non-parametric test was performed between the activity during the interstimulus interval
865 and during presentation of the preferred visual stimulus (Wilcoxon Rank Sum test, $p < 0.05$).

866 Neurons were included in further analyses if they were visually responsive both before and after
867 photoactivation, and if they were determined to be successfully photoactivated.

868 Orientation selectivity was calculated using a calculation of the global orientation selectivity index
869 (gOSI):

870 $gOSI = |(\sum R(\theta) \times e^{2i\theta}) / \sum R(\theta)|$

871 Where $R(qk)$ is the response to angle qk . To calculate the population average, responses of each
872 cell were normalized to their maximum response and artificially centered to 0. Normalized
873 responses of cells were averaged and fitted using a double Gaussian:

874 $R = C + R_{pref} \times e^{(-(\theta - \theta_{pref})^2 / (2 * \sigma^2))} + R_{null} \times e^{(-(\theta_{null} - \theta_{pref})^2 / (2 * \sigma^2))}$

875 Where C is a constant offset, R_{pref} is the response to the stimulus that produced the maximum
876 response and R_{null} is the mean response to the opposite direction: Orientation preference was
877 calculated as the orientation that elicited the highest dF/F value according to the fit of the gaussian
878 tuning curves.

879

880 **Image denoising**

881 To correct for vertical scanning artifacts, we utilized combined wavelet and Fourier filters
882 described in ref.¹¹⁸ [github: <https://github.com/DHI-GRAS/rmstripes>]. Symlet 20 wavelets were
883 used with varying levels of decomposition (2-5) for discrete wavelet transform to perform vertical
884 striping correction in static images.

885

886 ***In vivo* and *ex vivo* image registration**

887 The *in vivo* and *ex vivo* images were transformed into 3D volumetric images for registration. The
888 *in vivo* sequential images were concatenated across the z direction, i.e., depth, stacking the 2D
889 images into a volumetric representation using MATLAB. The *ex vivo* images composed of 2D
890 slices in each section were concatenated into 3D volumetric data using a stitching algorithm
891 developed as a precursor for automatic *ex vivo* and *in vivo* registration¹⁰⁶
892 [github: https://github.com/ShuonanChen/multimodal_image_registration]. The discontinuity
893 between *ex vivo* sections result in an unknown spatial correlation between them, requiring
894 registration between sections. Common cells between sections (i.e., sections one and two) were
895 used as reference markers for registration. The common cells were manually selected using a
896 Napari GUI in Python and were utilized as reference markers to inform the scaling and affine
897 transformations to be applied. The scaling and affine transformations were run automatically,
898 transforming the second section to align with the first section. In the scaling transformation, the
899 relative distances between cells in a section were compared to the cells in the first section, inducing
900 an enlargement or shrinkage of the second section to match the first. In the affine transformation,
901 the second section was geometrically transformed to align correctly with the first section. The
902 transformations were obtained and applied to each slice in each section, and then each slice was
903 concatenated together across the z direction to form a volumetric image.

904

905 The *in vivo* and *ex vivo* 3D images were then adjusted to have a uniform pixel size in all dimensions
906 (1 μ m in x,y and z), ensuring matching FOVs, and equivalent resolution across both images. Time-
907 averaged representations of *in vivo* and *ex vivo* volumetric stacks were attained by employing
908 maximum intensity projection (MIP) representations in FIJI, compressing the stacks into 2D
909 images¹¹⁹. The *in vivo* and *ex vivo* registration was carried out using a non-rigid registration
910 algorithm for the (i) 3D volumetric stacks and (ii) MIP (2D) images. All cells common to both *in*
911 *vivo* and *ex vivo* images were manually selected as the centroid of each cell using a Napari GUI in
912 Python. The common cells were utilized as features to inform the scaling, affine transformation,
913 and deformation transformation, which were applied to the *ex vivo* image. The scaling and affine
914 transformations were run automatically. In the scaling transformation, the distances between the
915 cells in the *ex vivo* image and matching cells in *in vivo* induce enlargement or shrinking of the *ex*
916 *vivo* image to match the *in vivo* image. In the affine transformation, the *ex vivo* image was
917 geometrically transformed to align with the *in vivo* image using the matching cells. The images in
918 the GUI are updated to reflect the changes induced by the scaling and affine transformation. The
919 deformation transformation uses a vector field, smoothed with Gaussian filtering, to move cells
920 and deform the image, ensuring features in the transformed *ex vivo* image align with the *in vivo*
921 image. The deformation transformation was iteratively employed, beginning with a Gaussian
922 kernel size of 100, reducing to a kernel size of less than 10, with the user inspecting the alignment
923 and making manual adjustments to the cell centroid position in the GUI. The completed
924 transformed *ex vivo* image was then overlaid with the *in vivo* image.

925

926 **RNA-sequencing data analysis**

927 Sequencing data from the Illumina Sequencer was first post-processed through the Illumina
928 DRAGEN secondary analysis pipeline to de-multiplex based on a unique index for each sample.
929 RNA-seq reads were aligned to the mouse genome (mm39) using STAR¹²⁰. Unique reads were
930 counted using HTSeq¹²¹. Gene counts were then normalized with trimmed mean of M values
931 (TMM) normalization. HTSeq generated reads were then analyzed for differential expression
932 using PyDESeq2¹¹⁵. Following HTSeq counts, any genes with expression in less than 3 samples
933 were discarded. FDR adjusted p values were used to determine significantly different genes. Both
934 ‘place’ and ‘silent’ cell samples were analyzed against randomly tagged, function-blind, and sex-
935 matched samples generated from mouse CA1 tissue in the same way as described in this methods
936 section above. The same comparisons were made to identify differentially expressed genes for
937 ‘place’ versus ‘random’, and ‘silent’ versus ‘random’. Within this ‘random’ dataset, male-female
938 samples were compared to identify differentially expressed genes influenced by sex. All DEGs
939 from these comparisons were cross-referenced to find common hits.

940

941 **Gene set enrichment analysis**

942 Gene set enrichment analysis was performed on HTSeq-generated counts using the gseapy
943 package¹²² in Python 3.11. Enrichment of the fifty hallmark pathways from the molecular
944 signatures database for *Mus musculus* (version 2023.2) was compared in place and silent cells.
945 Comparisons were done with t-test and 1000 permutations.

946

947 **RNAscope FISH signal quantification and statistical analysis**

948 Cell detection was performed using Cellpose, which identified individual cells based on DAPI
949 nuclear staining. This segmentation was manually curated. The detection and quantification of
950 RNAscope probe signals was performed using QuPath’s Subcellular Detection tool (version 0.5.1).
951 The detection threshold was set to ensure accurate identification of signal dots. To compare mean
952 RNA expression levels between tagged and non-tagged cells, a Mann-Whitney U Test was used.
953 For non-tagged control cells, a random subset was selected from the same tissue sections and
954 CA1sublayer as the tagged cells, with the number of control cells matched to the number of tagged
955 cells for each animal.

956

957 **Acknowledgments**

958 We thank Ira Schieren and Max Wallach (Columbia, Zuckerman Institute, ZI) and Dr. Efrat Hagai
959 (Flow Cytometry Unit, Weizmann Institute of Science) for help with FACS, Columbia University
960 Herbert Irvine Comprehensive Cancer Center Molecular Pathology Shared Resources for help with
961 the Bioanalyzer, the Bendesky lab in ZI and Dr. Hadas Keren-Shaul, Revital Ronen at the
962 Weizmann, Nancy and Stephen Grand Israel National Center (G-INCPM) for help with RNA-
963 sequencing, George Zakka (Losonczy Lab) for technical support, Erica Rodriguez (Salzman lab)
964 in ZI for help with tissue processing, the Lomvardas lab in ZI for sequencing advice and help, the
965 Gogos lab in ZI for molecular bench space, the Polleux lab in ZI for help with cell counter and
966 confocal microscopy. We thank Franck Polleux, Joseph Gogos, Steven A. Siegelbaum, and Darcy
967 Peterka (Columbia, ZI) for feedback on the manuscript.

968

969 **Funding**

970 SAH is supported by the Burroughs Wellcome Fund. DK is supported by a fellowship from the
971 Israel Ministry of Absorption (IMOAb) and by the Horowitz Foundation. AL is supported by
972 NIMHR01MH124047, NIMHR01MH124867, NINDSR01NS121106, NINDSU01NS115530,
973 NINDSR01NS133381, NINDSR01NS131728, NIARF1AG080818. IS is supported by an ISF
974 personal grant (2354/19) and a BSF US-Israel binational grant (2021281) and he is the incumbent
975 of the Friends and Linda and Richard Price Career Development Chair and a scholar in the
976 Zuckerman STEM leadership program.

977

978 **Author contributions:**

979 Conceptualization: JS, BN, DK, AL, IS
980 Methodology: JS, BN, DK, BR, SAH, ET, KCK, MECP, HCY, BMS, AX
981 Investigation: JS, BR
982 Software: BR, JS, TSM, CKO, EV
983 Formal analysis: JS, BR, TSM, ET, AL
984 Validation: JS, BN, DK, KCK, BR
985 Visualization: JS, BR, TSM, SAH, CKO, ET, MECP, KC-KM
986 Data curation: JS, BR, ET, TSM
987 Funding acquisition: AL, IS
988 Resources: AL, IS
989 Project administration: AL, IS
990 Supervision: AL, IS
991 Writing – original draft: JS, BN, BR, TSM, AL, IS
992 Writing – review & editing: all authors

993 **Competing interests:** Authors declare that they have no competing interests.

994

995 **Data and material availability** All data, code, and materials used to generate figures and perform
996 statistical tests are available at Zenodo or NWB upon publication. RNA-seq data will be made
997 freely available on NCBI GEO upon acceptance of our manuscript. Accession numbers for
998 publicly available reagents are included in supplementary materials and methods.

References

999 1. Zeng, H. (2022). What is a cell type and how to define it? *Cell* *185*, 2739–2755.
1000 <https://doi.org/10.1016/j.cell.2022.06.031>.

1001 2. Macosko, E.Z., Basu, A., Satija, R., Nemesh, J., Shekhar, K., Goldman, M., Tirosh, I., Bialas,
1002 A.R., Kamitaki, N., Martersteck, E.M., et al. (2015). Highly Parallel Genome-wide
1003 Expression Profiling of Individual Cells Using Nanoliter Droplets. *Cell* *161*, 1202–1214.
1004 <https://doi.org/10.1016/j.cell.2015.05.002>.

1005 3. Tasic, B., Menon, V., Nguyen, T.N., Kim, T.K., Jarsky, T., Yao, Z., Levi, B., Gray, L.T., Sorensen,
1006 S.A., Dolbeare, T., et al. (2016). Adult mouse cortical cell taxonomy revealed by single cell
1007 transcriptomics. *Nat Neurosci* *19*, 335–346. <https://doi.org/10.1038/nn.4216>.

1008 4. Zeisel, A., Muñoz-Manchado, A.B., Codeluppi, S., Lönnerberg, P., La Manno, G., Juréus, A.,
1009 Marques, S., Munguba, H., He, L., Betsholtz, C., et al. (2015). Cell types in the mouse cortex
1010 and hippocampus revealed by single-cell RNA-seq. *Science* *347*, 1138–1142.
1011 <https://doi.org/10.1126/science.aaa1934>.

1012 5. Harris, K.D., Hochgerner, H., Skene, N.G., Magno, L., Katona, L., Bengtsson Gonzales, C.,
1013 Somogyi, P., Kessaris, N., Linnarsson, S., and Hjerling-Leffler, J. (2018). Classes and
1014 continua of hippocampal CA1 inhibitory neurons revealed by single-cell transcriptomics.
1015 *PLoS Biol* *16*, e2006387. <https://doi.org/10.1371/journal.pbio.2006387>.

1016 6. Piwecka, M., Rajewsky, N., and Rybak-Wolf, A. (2023). Single-cell and spatial transcriptomics:
1017 deciphering brain complexity in health and disease. *Nat Rev Neurol* *19*, 346–362.
1018 <https://doi.org/10.1038/s41582-023-00809-y>.

1019 7. Zhang, M., Pan, X., Jung, W., Halpern, A.R., Eichhorn, S.W., Lei, Z., Cohen, L., Smith, K.A.,
1020 Tasic, B., Yao, Z., et al. (2023). Molecularly defined and spatially resolved cell atlas of the
1021 whole mouse brain. *Nature* *624*, 343–354. <https://doi.org/10.1038/s41586-023-06808-9>.

1022 8. Moses, L., and Pachter, L. (2022). Museum of spatial transcriptomics. *Nat Methods* *19*, 534–
1023 546. <https://doi.org/10.1038/s41592-022-01409-2>.

1024 9. Cadwell, C.R., Scala, F., Li, S., Livrizzi, G., Shen, S., Sandberg, R., Jiang, X., and Tolias, A.S.
1025 (2017). Multimodal profiling of single-cell morphology, electrophysiology, and gene
1026 expression using Patch-seq. *Nat Protoc* *12*, 2531–2553.
1027 <https://doi.org/10.1038/nprot.2017.120>.

1028 10. Cossell, L., Iacaruso, M.F., Muir, D.R., Houlton, R., Sader, E.N., Ko, H., Hofer, S.B., and Mrsic-
1029 Flogel, T.D. (2015). Functional organization of excitatory synaptic strength in primary
1030 visual cortex. *Nature* *518*, 399–403. <https://doi.org/10.1038/nature14182>.

1031 11. Ko, H., Hofer, S.B., Pichler, B., Buchanan, K.A., Sjöström, P.J., and Mrsic-Flogel, T.D. (2011).
1032 Functional specificity of local synaptic connections in neocortical networks. *Nature* **473**,
1033 87–91. <https://doi.org/10.1038/nature09880>.

1034 12. Scala, F., Kobak, D., Bernabucci, M., Bernaerts, Y., Cadwell, C.R., Castro, J.R., Hartmanis, L.,
1035 Jiang, X., Latschnig, S., Miranda, E., et al. (2021). Phenotypic variation of transcriptomic cell
1036 types in mouse motor cortex. *Nature* **598**, 144–150. [https://doi.org/10.1038/s41586-020-2907-3](https://doi.org/10.1038/s41586-020-
1037 2907-3).

1038 13. Bock, D.D., Lee, W.-C.A., Kerlin, A.M., Andermann, M.L., Hood, G., Wetzel, A.W., Yurgenson,
1039 S., Soucy, E.R., Kim, H.S., and Reid, R.C. (2011). Network anatomy and in vivo physiology of
1040 visual cortical neurons. *Nature* **471**, 177–182. <https://doi.org/10.1038/nature09802>.

1041 14. Taniguchi, H., He, M., Wu, P., Kim, S., Paik, R., Sugino, K., Kvitsani, D., Fu, Y., Lu, J., Lin, Y., et
1042 al. (2011). A Resource of Cre Driver Lines for Genetic Targeting of GABAergic Neurons in
1043 Cerebral Cortex. *Neuron* **71**, 995–1013. <https://doi.org/10.1016/j.neuron.2011.07.026>.

1044 15. Vormstein-Schneider, D., Lin, J.D., Pelkey, K.A., Chittajallu, R., Guo, B., Arias-Garcia, M.A.,
1045 Allaway, K., Sakopoulos, S., Schneider, G., Stevenson, O., et al. (2020). Viral manipulation
1046 of functionally distinct interneurons in mice, non-human primates and humans. *Nat
1047 Neurosci* **23**, 1629–1636. <https://doi.org/10.1038/s41593-020-0692-9>.

1048 16. O'Toole, S.M., Oyibo, H.K., and Keller, G.B. (2023). Molecularly targetable cell types in
1049 mouse visual cortex have distinguishable prediction error responses. *Neuron* **111**, 2918–
1050 2928.e8. <https://doi.org/10.1016/j.neuron.2023.08.015>.

1051 17. Condylis, C., Ghanbari, A., Manjrekar, N., Bistrong, K., Yao, S., Yao, Z., Nguyen, T.N., Zeng,
1052 H., Tasic, B., and Chen, J.L. (2022). Dense functional and molecular readout of a circuit hub
1053 in sensory cortex. *Science* **375**, eabl5981. <https://doi.org/10.1126/science.abl5981>.

1054 18. Bugeon, S., Duffield, J., Dipoppa, M., Ritoux, A., Prankerd, I., Nicoloutsopoulos, D., Orme, D.,
1055 Shinn, M., Peng, H., Forrest, H., et al. (2022). A transcriptomic axis predicts state
1056 modulation of cortical interneurons. *Nature* **607**, 330–338.
1057 <https://doi.org/10.1038/s41586-022-04915-7>.

1058 19. Geiller, T., Vancura, B., Terada, S., Troullinou, E., Chavlis, S., Tsagkatakis, G., Tsakalides, P.,
1059 Ócsai, K., Poirazi, P., Rózsa, B.J., et al. (2020). Large-Scale 3D Two-Photon Imaging of
1060 Molecularly Identified CA1 Interneuron Dynamics in Behaving Mice. *Neuron* **108**, 968–
1061 983.e9. <https://doi.org/10.1016/j.neuron.2020.09.013>.

1062 20. Vancura, B., Geiller, T., Grosmark, A., Zhao, V., and Losonczy, A. (2023). Inhibitory control of
1063 sharp-wave ripple duration during learning in hippocampal recurrent networks. *Nat
1064 Neurosci*, 1–10. <https://doi.org/10.1038/s41593-023-01306-7>.

1065 21. Cohen-Kashi Malina, K., Tsivourakis, E., Kushinsky, D., Apelblat, D., Shtiglitz, S., Zohar, E.,
1066 Sokoletsky, M., Tasaka, G., Mizrahi, A., Lampl, I., et al. (2021). NDNF interneurons in layer

1067 1 gain-modulate whole cortical columns according to an animal's behavioral state. *Neuron*
1068 109, 2150-2164.e5. <https://doi.org/10.1016/j.neuron.2021.05.001>.

1069 22. Hansel, D., and Vreeswijk, C. van (2012). The Mechanism of Orientation Selectivity in
1070 Primary Visual Cortex without a Functional Map. *J. Neurosci.* 32, 4049–4064.
1071 <https://doi.org/10.1523/JNEUROSCI.6284-11.2012>.

1072 23. Hirokawa, J., Vaughan, A., Masset, P., Ott, T., and Kepecs, A. (2019). Frontal cortex neuron
1073 types categorically encode single decision variables. *Nature* 576, 446–451.
1074 <https://doi.org/10.1038/s41586-019-1816-9>.

1075 24. Mancinelli, S., and Lodato, S. (2018). Decoding neuronal diversity in the developing cerebral
1076 cortex: from single cells to functional networks. *Current Opinion in Neurobiology* 53, 146–
1077 155. <https://doi.org/10.1016/j.conb.2018.08.001>.

1078 25. Ohki, K., and Reid, R.C. (2007). Specificity and randomness in the visual cortex. *Current
1079 Opinion in Neurobiology* 17, 401–407. <https://doi.org/10.1016/j.conb.2007.07.007>.

1080 26. Peng, H., Xie, P., Liu, L., Kuang, X., Wang, Y., Qu, L., Gong, H., Jiang, S., Li, A., Ruan, Z., et al.
1081 (2021). Morphological diversity of single neurons in molecularly defined cell types. *Nature*
1082 598, 174–181. <https://doi.org/10.1038/s41586-021-03941-1>.

1083 27. Treves, A., and Rolls, E.T. (1994). Computational analysis of the role of the hippocampus in
1084 memory. *Hippocampus* 4, 374–391. <https://doi.org/10.1002/hipo.450040319>.

1085 28. Buzsáki, G., and Mizuseki, K. (2014). The log-dynamic brain: how skewed distributions affect
1086 network operations. *Nat Rev Neurosci* 15, 264–278. <https://doi.org/10.1038/nrn3687>.

1087 29. Cembrowski, M.S., Bachman, J.L., Wang, L., Sugino, K., Shields, B.C., and Spruston, N.
1088 (2016). Spatial Gene-Expression Gradients Underlie Prominent Heterogeneity of CA1
1089 Pyramidal Neurons. *Neuron* 89, 351–368. <https://doi.org/10.1016/j.neuron.2015.12.013>.

1090 30. Mallory, C.S., and Giocomo, L.M. (2018). Heterogeneity in hippocampal place coding.
1091 *Current Opinion in Neurobiology* 49, 158–167.
1092 <https://doi.org/10.1016/j.conb.2018.02.014>.

1093 31. Pettit, N.L., Yap, E.-L., Greenberg, M.E., and Harvey, C.D. (2022). Fos ensembles encode and
1094 shape stable spatial maps in the hippocampus. *Nature* 609, 327–334.
1095 <https://doi.org/10.1038/s41586-022-05113-1>.

1096 32. Soltesz, I., and Losonczy, A. (2018). CA1 pyramidal cell diversity enabling parallel
1097 information processing in the hippocampus. *Nat Neurosci* 21, 484–493.
1098 <https://doi.org/10.1038/s41593-018-0118-0>.

1099 33. Sosa, M., Gillespie, A.K., and Frank, L.M. (2018). Neural Activity Patterns Underlying Spatial
1100 Coding in the Hippocampus. In *Behavioral Neuroscience of Learning and Memory*, R. E.

1101 Clark and S. J. Martin, eds. (Springer International Publishing), pp. 43–100.
1102 https://doi.org/10.1007/7854_2016_462.

1103 34. Tanaka, K.Z., He, H., Tomar, A., Niisato, K., Huang, A.J.Y., and McHugh, T.J. (2018). The
1104 hippocampal engram maps experience but not place. *Science* *361*, 392–397.
1105 <https://doi.org/10.1126/science.aat5397>.

1106 35. Ziv, Y., Burns, L.D., Cocker, E.D., Hamel, E.O., Ghosh, K.K., Kitch, L.J., Gamal, A.E., and
1107 Schnitzer, M.J. (2013). Long-term dynamics of CA1 hippocampal place codes. *Nat Neurosci*
1108 *16*, 264–266. <https://doi.org/10.1038/nn.3329>.

1109 36. Lee, J.S., Briguglio, J.J., Cohen, J.D., Romani, S., and Lee, A.K. (2020). The Statistical Structure
1110 of the Hippocampal Code for Space as a Function of Time, Context, and Value. *Cell* *183*,
1111 620-635.e22. <https://doi.org/10.1016/j.cell.2020.09.024>.

1112 37. Kentros, C.G., Agnihotri, N.T., Streater, S., Hawkins, R.D., and Kandel, E.R. (2004). Increased
1113 Attention to Spatial Context Increases Both Place Field Stability and Spatial Memory.
1114 *Neuron* *42*, 283–295. [https://doi.org/10.1016/S0896-6273\(04\)00192-8](https://doi.org/10.1016/S0896-6273(04)00192-8).

1115 38. Grosmark, A.D., Sparks, F.T., Davis, M.J., and Losonczy, A. (2021). Reactivation predicts the
1116 consolidation of unbiased long-term cognitive maps. *Nat Neurosci* *24*, 1574–1585.
1117 <https://doi.org/10.1038/s41593-021-00920-7>.

1118 39. Keinath, A.T., Mosser, C.-A., and Brandon, M.P. (2022). The representation of context in
1119 mouse hippocampus is preserved despite neural drift. *Nat Commun* *13*, 2415.
1120 <https://doi.org/10.1038/s41467-022-30198-7>.

1121 40. Colgin, L.L., Moser, E.I., and Moser, M.-B. (2008). Understanding memory through
1122 hippocampal remapping. *Trends in Neurosciences* *31*, 469–477.
1123 <https://doi.org/10.1016/j.tins.2008.06.008>.

1124 41. Moeyaert, B., Holt, G., Madangopal, R., Perez-Alvarez, A., Fearey, B.C., Trojanowski, N.F.,
1125 Ledderose, J., Zolnik, T.A., Das, A., Patel, D., et al. (2018). Improved methods for marking
1126 active neuron populations. *Nat Commun* *9*, 4440. <https://doi.org/10.1038/s41467-018-06935-2>.

1128 42. Hyun, J.H., Nagahama, K., Namkung, H., Mignocchi, N., Roh, S.-E., Hannan, P., Krüssel, S.,
1129 Kwak, C., McElroy, A., Liu, B., et al. (2022). Tagging active neurons by soma-targeted Cal-
1130 Light. *Nat Commun* *13*, 7692. <https://doi.org/10.1038/s41467-022-35406-y>.

1131 43. Mocle, A.J., Ramsaran, A.I., Jacob, A.D., Rashid, A.J., Luchetti, A., Tran, L.M., Richards, B.A.,
1132 Frankland, P.W., and Josselyn, S.A. (2024). Excitability mediates allocation of pre-
1133 configured ensembles to a hippocampal engram supporting contextual conditioned threat
1134 in mice. *Neuron* *112*, 1487-1497.e6. <https://doi.org/10.1016/j.neuron.2024.02.007>.

1135 44. DeNardo, L.A., Liu, C.D., Allen, W.E., Adams, E.L., Friedmann, D., Fu, L., Guenthner, C.J.,
1136 Tessier-Lavigne, M., and Luo, L. (2019). Temporal evolution of cortical ensembles
1137 promoting remote memory retrieval. *Nat Neurosci* 22, 460–469.
1138 <https://doi.org/10.1038/s41593-018-0318-7>.

1139 45. Guenthner, C.J., Miyamichi, K., Yang, H.H., Heller, H.C., and Luo, L. (2013). Permanent
1140 Genetic Access to Transiently Active Neurons via TRAP: Targeted Recombination in Active
1141 Populations. *Neuron* 78, 773–784. <https://doi.org/10.1016/j.neuron.2013.03.025>.

1142 46. Lee, D., Hyun, J.H., Jung, K., Hannan, P., and Kwon, H.-B. (2017). A calcium- and light-gated
1143 switch to induce gene expression in activated neurons. *Nat Biotechnol* 35, 858–863.
1144 <https://doi.org/10.1038/nbt.3902>.

1145 47. Sørensen, A.T., Cooper, Y.A., Baratta, M.V., Weng, F.-J., Zhang, Y., Ramamoorthi, K., Fropf,
1146 R., LaVerriere, E., Xue, J., Young, A., et al. (2016). A robust activity marking system for
1147 exploring active neuronal ensembles. *eLife* 5, e13918.
1148 <https://doi.org/10.7554/eLife.13918>.

1149 48. Datta, S.R., Vasconcelos, M.L., Ruta, V., Luo, S., Wong, A., Demir, E., Flores, J., Balonze, K.,
1150 Dickson, B.J., and Axel, R. (2008). The *Drosophila* pheromone cVA activates a sexually
1151 dimorphic neural circuit. *Nature* 452, 473–477. <https://doi.org/10.1038/nature06808>.

1152 49. Lien, A.D., and Scanziani, M. (2011). In vivo Labeling of Constellations of Functionally
1153 Identified Neurons for Targeted in vitro Recordings. *Front Neural Circuits* 5, 16.
1154 <https://doi.org/10.3389/fncir.2011.00016>.

1155 50. Lee, D., Kume, M., and Holy, T.E. (2019). Sensory coding mechanisms revealed by optical
1156 tagging of physiologically defined neuronal types. *Science* 366, 1384–1389.
1157 <https://doi.org/10.1126/science.aax8055>.

1158 51. Dana, H., Sun, Y., Mohar, B., Hulse, B.K., Kerlin, A.M., Hasseman, J.P., Tsegaye, G., Tsang, A.,
1159 Wong, A., Patel, R., et al. (2019). High-performance calcium sensors for imaging activity in
1160 neuronal populations and microcompartments. *Nat Methods* 16, 649–657.
1161 <https://doi.org/10.1038/s41592-019-0435-6>.

1162 52. Scheyltjens, I., Laramée, M.-E., Van den Haute, C., Gijsbers, R., Debys, Z., Baekelandt, V.,
1163 Vreysen, S., and Arckens, L. (2015). Evaluation of the expression pattern of rAAV2/1, 2/5,
1164 2/7, 2/8, and 2/9 serotypes with different promoters in the mouse visual cortex. *Journal of
1165 Comparative Neurology* 523, 2019–2042. <https://doi.org/10.1002/cne.23819>.

1166 53. Geiller, T., Priestley, J.B., and Losonczy, A. (2023). A local circuit-basis for spatial navigation
1167 and memory processes in hippocampal area CA1. *Current Opinion in Neurobiology* 79,
1168 102701. <https://doi.org/10.1016/j.conb.2023.102701>.

1169 54. Katona, G., Szalay, G., Maák, P., Kaszás, A., Veress, M., Hillier, D., Chiovini, B., Vizi, E.S.,
1170 Roska, B., and Rózsa, B. (2012). Fast two-photon in vivo imaging with three-dimensional

1171 random-access scanning in large tissue volumes. *Nat Methods* 9, 201–208.
1172 <https://doi.org/10.1038/nmeth.1851>.

1173 55. Apelblat, D., Roethler, O., Bitan, L., Keren-Shaul, H., and Spiegel, I. (2022). Meso-seq for in-
1174 depth transcriptomics in ultra-low amounts of FACS-purified neuronal nuclei. *Cell Reports*
1175 *Methods* 2, 100259. <https://doi.org/10.1016/j.crmeth.2022.100259>.

1176 56. Roethler, O., Zohar, E., Cohen-Kashi Malina, K., Bitan, L., Gabel, H.W., and Spiegel, I. (2023).
1177 Single genomic enhancers drive experience-dependent GABAergic plasticity to maintain
1178 sensory processing in the adult cortex. *Neuron* 111, 2693–2708.e8.
1179 <https://doi.org/10.1016/j.neuron.2023.05.026>.

1180 57. O'Keefe, J., and Dostrovsky, J. (1971). The hippocampus as a spatial map. Preliminary
1181 evidence from unit activity in the freely-moving rat. *Brain Research* 34, 171–175.
1182 [https://doi.org/10.1016/0006-8993\(71\)90358-1](https://doi.org/10.1016/0006-8993(71)90358-1).

1183 58. Witharana, W. k. I., Cardiff, J., Chawla, M. k., Xie, J. y., Alme, C. b., Eckert, M., Lapointe, V.,
1184 Demchuk, A., Maurer, A. p., Trivedi, V., et al. (2016). Nonuniform allocation of
1185 hippocampal neurons to place fields across all hippocampal subfields. *Hippocampus* 26,
1186 1328–1344. <https://doi.org/10.1002/hipo.22609>.

1187 59. Cembrowski, M.S. (2019). Single-cell transcriptomics as a framework and roadmap for
1188 understanding the brain. *Journal of Neuroscience Methods* 326, 108353.
1189 <https://doi.org/10.1016/j.jneumeth.2019.108353>.

1190 60. Yao, Z., Velthoven, C.T.J. van, Nguyen, T.N., Goldy, J., Sedeno-Cortes, A.E., Baftizadeh, F.,
1191 Bertagnolli, D., Casper, T., Chiang, M., Crichton, K., et al. (2021). A taxonomy of
1192 transcriptomic cell types across the isocortex and hippocampal formation. *Cell* 184, 3222–
1193 3241.e26. <https://doi.org/10.1016/j.cell.2021.04.021>.

1194 61. Rich, P.D., Liaw, H.-P., and Lee, A.K. (2014). Large environments reveal the statistical
1195 structure governing hippocampal representations. *Science* 345, 814–817.
1196 <https://doi.org/10.1126/science.1255635>.

1197 62. Thompson, L.T., and Best, P.J. (1989). Place cells and silent cells in the hippocampus of
1198 freely-behaving rats. *J. Neurosci.* 9, 2382–2390. <https://doi.org/10.1523/JNEUROSCI.09-07-02382.1989>.

1200 63. Wilson, M.A., and McNaughton, B.L. (1993). Dynamics of the Hippocampal Ensemble Code
1201 for Space. *Science* 261, 1055–1058. <https://doi.org/10.1126/science.8351520>.

1202 64. Zaremba, J.D., Diamantopoulou, A., Danielson, N.B., Grosmark, A.D., Kaifosh, P.W., Bowler,
1203 J.C., Liao, Z., Sparks, F.T., Gogos, J.A., and Losonczy, A. (2017). Impaired hippocampal place
1204 cell dynamics in a mouse model of the 22q11.2 deletion. *Nat Neurosci* 20, 1612–1623.
1205 <https://doi.org/10.1038/nn.4634>.

1206 65. Bowler, J.C., and Losonczy, A. (2023). Direct cortical inputs to hippocampal area CA1
1207 transmit complementary signals for goal-directed navigation. *Neuron* 0.
1208 <https://doi.org/10.1016/j.neuron.2023.09.013>.

1209 66. Bowler, J.C., Zakka, G., Yong, H.C., Li, W., Rao, B., Liao, Z., Priestley, J.B., and Losonczy, A.
1210 (2024). behaviorMate: An *Intranet* of Things Approach for Adaptable Control
1211 of Behavioral and Navigation-Based Experiments. *bioRxiv*, 2023.12.04.569989.
1212 <https://doi.org/10.1101/2023.12.04.569989>.

1213 67. Priestley, J.B., Bowler, J.C., Rolotti, S.V., Fusi, S., and Losonczy, A. (2022). Signatures of rapid
1214 plasticity in hippocampal CA1 representations during novel experiences. *Neuron*,
1215 S0896627322002628. <https://doi.org/10.1016/j.neuron.2022.03.026>.

1216 68. Rolotti, S.V., Ahmed, M.S., Szoboszlay, M., Geiller, T., Negrean, A., Blockus, H., Gonzalez,
1217 K.C., Sparks, F.T., Solis Canales, A.S., Tuttman, A.L., et al. (2022). Local feedback inhibition
1218 tightly controls rapid formation of hippocampal place fields. *Neuron* 110, 783-794.e6.
1219 <https://doi.org/10.1016/j.neuron.2021.12.003>.

1220 69. Geiller, T., Sadeh, S., Rolotti, S.V., Blockus, H., Vancura, B., Negrean, A., Murray, A.J., Rózsa,
1221 B., Polleux, F., Clopath, C., et al. (2022). Local circuit amplification of spatial selectivity in
1222 the hippocampus. *Nature* 601, 105–109. <https://doi.org/10.1038/s41586-021-04169-9>.

1223 70. Jeon, B.B., Swain, A.D., Good, J.T., Chase, S.M., and Kuhlman, S.J. (2018). Feature selectivity
1224 is stable in primary visual cortex across a range of spatial frequencies. *Sci Rep* 8, 15288.
1225 <https://doi.org/10.1038/s41598-018-33633-2>.

1226 71. Cembrowski, M.S., Wang, L., Sugino, K., Shields, B.C., and Spruston, N. (2016). Hipposeq: a
1227 comprehensive RNA-seq database of gene expression in hippocampal principal neurons.
1228 *eLife* 5, e14997. <https://doi.org/10.7554/eLife.14997>.

1229 72. Bloodgood, B.L., Sharma, N., Browne, H.A., Trepman, A.Z., and Greenberg, M.E. (2013). The
1230 activity-dependent transcription factor NPAS4 regulates domain-specific inhibition. *Nature*
1231 503, 121–125. <https://doi.org/10.1038/nature12743>.

1232 73. Sheng, M., and Greenberg, M.E. (1990). The regulation and function of *c-fos* and other
1233 immediate early genes in the nervous system. *Neuron* 4, 477–485.
1234 [https://doi.org/10.1016/0896-6273\(90\)90106-P](https://doi.org/10.1016/0896-6273(90)90106-P).

1235 74. Spiegel, I., Mardinly, A.R., Gabel, H.W., Bazinet, J.E., Couch, C.H., Tzeng, C.P., Harmin, D.A.,
1236 and Greenberg, M.E. (2014). Npas4 Regulates Excitatory-Inhibitory Balance within Neural
1237 Circuits through Cell-Type-Specific Gene Programs. *Cell* 157, 1216–1229.
1238 <https://doi.org/10.1016/j.cell.2014.03.058>.

1239 75. Apoptosis: A Review of Programmed Cell Death - Susan Elmore, 2007
1240 <https://journals.sagepub.com/doi/10.1080/01926230701320337>.

1241 76. Xu, J., Burgoyn, P.S., and Arnold, A.P. (2002). Sex differences in sex chromosome gene
1242 expression in mouse brain. *Human Molecular Genetics* 11, 1409–1419.
1243 <https://doi.org/10.1093/hmg/11.12.1409>.

1244 77. Nichols, C.G., and Lopatin, A.N. (1997). INWARD RECTIFIER POTASSIUM CHANNELS. Annual
1245 Review of Physiology 59, 171–191. <https://doi.org/10.1146/annurev.physiol.59.1.171>.

1246 78. Reimann, F., and Ashcroft, F.M. (1999). Inwardly rectifying potassium channels. *Current
1247 Opinion in Cell Biology* 11, 503–508. [https://doi.org/10.1016/S0955-0674\(99\)80073-8](https://doi.org/10.1016/S0955-0674(99)80073-8).

1248 79. Shcherbatyy, V., Carson, J., Yaylaoglu, M., Jäckle, K., Grabbe, F., Brockmeyer, M., Yavuz, H.,
1249 and Eichele, G. (2015). A Digital Atlas of Ion Channel Expression Patterns in the Two-Week-
1250 Old Rat Brain. *Neuroinform* 13, 111–125. <https://doi.org/10.1007/s12021-014-9247-0>.

1251 80. Alkon, D.L., Epstein, H., Kuzirian, A., Bennett, M.C., and Nelson, T.J. (2005). Protein synthesis
1252 required for long-term memory is induced by PKC activation on days before associative
1253 learning. *Proceedings of the National Academy of Sciences* 102, 16432–16437.
1254 <https://doi.org/10.1073/pnas.0508001102>.

1255 81. Gottschall, P.E., and Howell, M.D. (2015). ADAMTS expression and function in central
1256 nervous system injury and disorders. *Matrix Biology* 44–46, 70–76.
1257 <https://doi.org/10.1016/j.matbio.2015.01.014>.

1258 82. Epsztein, J., Brecht, M., and Lee, A.K. (2011). Intracellular Determinants of Hippocampal
1259 CA1 Place and Silent Cell Activity in a Novel Environment. *Neuron* 70, 109–120.
1260 <https://doi.org/10.1016/j.neuron.2011.03.006>.

1261 83. Santoni, G., Astori, S., Leleu, M., Glauser, L., Zamora, S.A., Schioppa, M., Tarulli, I., Sandi, C.,
1262 and Gräff, J. (2024). Chromatin plasticity predetermines neuronal eligibility for memory
1263 trace formation. *Science* 385, eadg9982. <https://doi.org/10.1126/science.adg9982>.

1264 84. Yiu, A.P., Mercaldo, V., Yan, C., Richards, B., Rashid, A.J., Hsiang, H.-L.L., Pressey, J.,
1265 Mahadevan, V., Tran, M.M., Kushner, S.A., et al. (2014). Neurons Are Recruited to a
1266 Memory Trace Based on Relative Neuronal Excitability Immediately before Training.
1267 *Neuron* 83, 722–735. <https://doi.org/10.1016/j.neuron.2014.07.017>.

1268 85. Josselyn, S.A., and Frankland, P.W. (2018). Memory Allocation: Mechanisms and Function.
1269 Annual Review of Neuroscience 41, 389–413. <https://doi.org/10.1146/annurev-neuro-080317-061956>.

1271 86. Sano, Y., Shobe, J.L., Zhou, M., Huang, S., Shuman, T., Cai, D.J., Golshani, P., Kamata, M., and
1272 Silva, A.J. (2014). CREB Regulates Memory Allocation in the Insular Cortex. *Current Biology*
1273 24, 2833–2837. <https://doi.org/10.1016/j.cub.2014.10.018>.

1274 87. Mizuseki, K., and Buzsáki, G. (2013). Preconfigured, Skewed Distribution of Firing Rates in
1275 the Hippocampus and Entorhinal Cortex. *Cell Reports* 4, 1010–1021.
1276 <https://doi.org/10.1016/j.celrep.2013.07.039>.

1277 88. Alme, C.B., Miao, C., Jezek, K., Treves, A., Moser, E.I., and Moser, M.-B. (2014). Place cells in
1278 the hippocampus: Eleven maps for eleven rooms. *Proceedings of the National Academy of
1279 Sciences* 111, 18428–18435. <https://doi.org/10.1073/pnas.1421056111>.

1280 89. Dragoi, G., and Tonegawa, S. (2011). Preplay of future place cell sequences by hippocampal
1281 cellular assemblies. *Nature* 469, 397–401. <https://doi.org/10.1038/nature09633>.

1282 90. Dragoi, G., and Tonegawa, S. (2014). Selection of preconfigured cell assemblies for
1283 representation of novel spatial experiences. *Philosophical Transactions of the Royal
1284 Society B: Biological Sciences* 369, 20120522. <https://doi.org/10.1098/rstb.2012.0522>.

1285 91. Grosmark, A.D., and Buzsáki, G. (2016). Diversity in neural firing dynamics supports both
1286 rigid and learned hippocampal sequences. *Science* 351, 1440–1443.
1287 <https://doi.org/10.1126/science.aad1935>.

1288 92. Huszár, R., Zhang, Y., Blockus, H., and Buzsáki, G. (2022). Preconfigured dynamics in the
1289 hippocampus are guided by embryonic birthdate and rate of neurogenesis. *Nat Neurosci*
1290 25, 1201–1212. <https://doi.org/10.1038/s41593-022-01138-x>.

1291 93. Cossart, R., and Khazipov, R. (2022). How development sculpts hippocampal circuits and
1292 function. *Physiological Reviews* 102, 343–378.
1293 <https://doi.org/10.1152/physrev.00044.2020>.

1294 94. Donato, F., Jacobsen, R.I., Moser, M.-B., and Moser, E.I. (2017). Stellate cells drive
1295 maturation of the entorhinal-hippocampal circuit. *Science* 355, eaai8178.
1296 <https://doi.org/10.1126/science.aai8178>.

1297 95. Deguchi, Y., Donato, F., Galimberti, I., Cabuy, E., and Caroni, P. (2011). Temporally matched
1298 subpopulations of selectively interconnected principal neurons in the hippocampus. *Nat
1299 Neurosci* 14, 495–504. <https://doi.org/10.1038/nn.2768>.

1300 96. Kveim, V.A., Salm, L., Ulmer, T., Lahr, M., Kandler, S., Imhof, F., and Donato, F. (2024).
1301 Divergent recruitment of developmentally defined neuronal ensembles supports memory
1302 dynamics. *Science* 385, eadk0997. <https://doi.org/10.1126/science.adk0997>.

1303 97. Marissal, T., Bonifazi, P., Picardo, M.A., Nardou, R., Petit, L.F., Baude, A., Fishell, G.J., Ben-
1304 Ari, Y., and Cossart, R. (2012). Pioneer glutamatergic cells develop into a morpho-
1305 functionally distinct population in the juvenile CA3 hippocampus. *Nat Commun* 3, 1316.
1306 <https://doi.org/10.1038/ncomms2318>.

1307 98. Jovasevic, V., Wood, E.M., Cicvaric, A., Zhang, H., Petrovic, Z., Carboncino, A., Parker, K.K.,
1308 Bassett, T.E., Moltesen, M., Yamawaki, N., et al. (2024). Formation of memory assemblies

1309 through the DNA-sensing TLR9 pathway. *Nature* 628, 145–153.
1310 <https://doi.org/10.1038/s41586-024-07220-7>.

1311 99. Solstad, T., Boccara, C.N., Kropff, E., Moser, M.-B., and Moser, E.I. (2008). Representation of
1312 Geometric Borders in the Entorhinal Cortex. *Science* 322, 1865–1868.
1313 <https://doi.org/10.1126/science.1166466>.

1314 100. Taube, J.S., Muller, R.U., and Ranck, J.B. (1990). Head-direction cells recorded from the
1315 postsubiculum in freely moving rats. I. Description and quantitative analysis. *J. Neurosci.*
1316 10, 420–435. <https://doi.org/10.1523/JNEUROSCI.10-02-00420.1990>.

1317 101. Eichenbaum, H. (2014). Time cells in the hippocampus: a new dimension for mapping
1318 memories. *Nat Rev Neurosci* 15, 732–744. <https://doi.org/10.1038/nrn3827>.

1319 102. Driscoll, L.N., Duncker, L., and Harvey, C.D. (2022). Representational drift: Emerging
1320 theories for continual learning and experimental future directions. *Current Opinion in
1321 Neurobiology* 76, 102609. <https://doi.org/10.1016/j.conb.2022.102609>.

1322 103. Josselyn, S.A., and Tonegawa, S. (2020). Memory engrams: Recalling the past and
1323 imagining the future. *Science* 367, eaaw4325. <https://doi.org/10.1126/science.aaw4325>.

1324 104. Xu, S., Yang, H., Menon, V., Lemire, A.L., Wang, L., Henry, F.E., Turaga, S.C., and Sternson,
1325 S.M. (2020). Behavioral state coding by molecularly defined paraventricular hypothalamic
1326 cell type ensembles. *Science* 370, eabb2494. <https://doi.org/10.1126/science.abb2494>.

1327 105. Chen, K.H., Boettiger, A.N., Moffitt, J.R., Wang, S., and Zhuang, X. (2015). Spatially
1328 resolved, highly multiplexed RNA profiling in single cells. *Science* 348, aaa6090.
1329 <https://doi.org/10.1126/science.aaa6090>.

1330 106. Chen, S., Rao, B.Y., Herrlinger, S., Losonczy, A., Paninski, L., and Varol, E. (2023).
1331 Multimodal Microscopy Image Alignment Using Spatial and Shape Information and a
1332 Branch-and-Bound Algorithm. In ICASSP 2023 - 2023 IEEE International Conference on
1333 Acoustics, Speech and Signal Processing (ICASSP), pp. 1–5.
1334 <https://doi.org/10.1109/ICASSP49357.2023.10096185>.

1335 107. Rao, B.Y., Peterson, A.M., Kandror, E.K., Herrlinger, S., Losonczy, A., Paninski, L., Rizvi, A.H.,
1336 and Varol, E. (2021). Non-parametric Vignetting Correction for Sparse Spatial
1337 Transcriptomics Images. In Medical Image Computing and Computer Assisted Intervention
1338 – MICCAI 2021, M. de Bruijne, P. C. Cattin, S. Cotin, N. Padoy, S. Speidel, Y. Zheng, and C.
1339 Essert, eds. (Springer International Publishing), pp. 466–475. [https://doi.org/10.1007/978-3-030-87237-3_45](https://doi.org/10.1007/978-
1340 3-030-87237-3_45).

1341 108. Bittner, K.C., Milstein, A.D., Grienberger, C., Romani, S., and Magee, J.C. (2017). Behavioral
1342 time scale synaptic plasticity underlies CA1 place fields. *Science* 357, 1033–1036.
1343 <https://doi.org/10.1126/science.aan3846>.

1344 109. Magee, J.C., and Grienberger, C. (2020). Synaptic Plasticity Forms and Functions. *Annual*
1345 *Review of Neuroscience* **43**, 95–117. <https://doi.org/10.1146/annurev-neuro-090919-022842>.

1347 110. Xue, M., Atallah, B.V., and Scanziani, M. (2014). Equalizing excitation–inhibition ratios
1348 across visual cortical neurons. *Nature* **511**, 596–600.
1349 <https://doi.org/10.1038/nature13321>.

1350 111. Wright, W.J., Hedrick, N.G., and Komiyama, T. (2025). Distinct synaptic plasticity rules
1351 operate across dendritic compartments *in vivo* during learning. *Science* **388**, 322–328.
1352 <https://doi.org/10.1126/science.ads4706>.

1353 112. Kaifosh, P., Zaremba, J.D., Danielson, N.B., and Losonczy, A. (2014). SIMA: Python software
1354 for analysis of dynamic fluorescence imaging data. *Front. Neuroinform.* **8**.
1355 <https://doi.org/10.3389/fninf.2014.00080>.

1356 113. Pachitariu, M., Stringer, C., Dipoppa, M., Schröder, S., Rossi, L.F., Dalgleish, H., Carandini, M., and Harris, K.D. (2017). Suite2p: beyond 10,000 neurons with standard two-photon microscopy. *bioRxiv*, 061507. <https://doi.org/10.1101/061507>.

1359 114. Stringer, C., Wang, T., Michaelos, M., and Pachitariu, M. (2021). Cellpose: a generalist
1360 algorithm for cellular segmentation. *Nat Methods* **18**, 100–106.
1361 <https://doi.org/10.1038/s41592-020-01018-x>.

1362 115. Muzellec, B., Teleńczuk, M., Cabeli, V., and Andreux, M. (2023). PyDESeq2: a python
1363 package for bulk RNA-seq differential expression analysis. *Bioinformatics* **39**, btad547.
1364 <https://doi.org/10.1093/bioinformatics/btad547>.

1365 116. Friedrich, J., Zhou, P., and Paninski, L. (2017). Fast online deconvolution of calcium imaging
1366 data. *PLOS Computational Biology* **13**, e1005423.
1367 <https://doi.org/10.1371/journal.pcbi.1005423>.

1368 117. O’Hare, J.K., Gonzalez, K.C., Herrlinger, S.A., Hirabayashi, Y., Hewitt, V.L., Blockus, H.,
1369 Szoboszlay, M., Rolotti, S.V., Geiller, T.C., Negrean, A., et al. (2022). Compartment-specific
1370 tuning of dendritic feature selectivity by intracellular Ca²⁺ release. *Science* **375**,
1371 eabm1670. <https://doi.org/10.1126/science.abm1670>.

1372 118. Münch, B., Trtik, P., Marone, F., and Stampanoni, M. (2009). Stripe and ring artifact
1373 removal with combined wavelet — Fourier filtering. *Opt. Express*, **17**, 8567–8591.
1374 <https://doi.org/10.1364/OE.17.008567>.

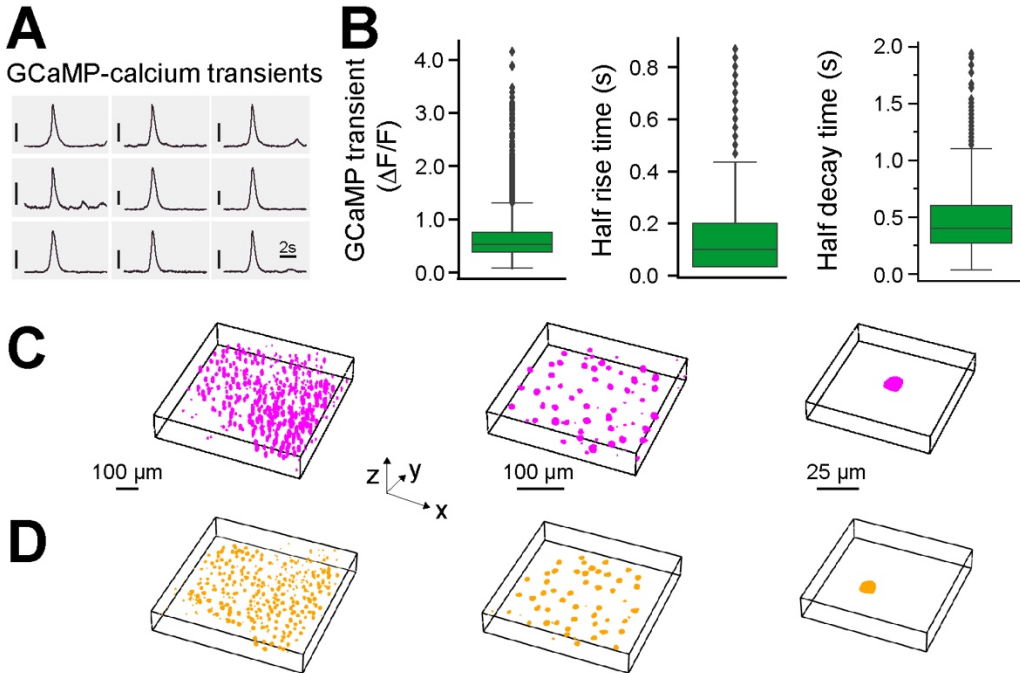
1375 119. Schindelin, J., Arganda-Carreras, I., Frise, E., Kaynig, V., Longair, M., Pietzsch, T., Preibisch,
1376 S., Rueden, C., Saalfeld, S., Schmid, B., et al. (2012). Fiji: an open-source platform for
1377 biological-image analysis. *Nature Methods* **9**, 676–682.
1378 <https://doi.org/10.1038/nmeth.2019>.

1379 120. Dobin, A., Davis, C.A., Schlesinger, F., Drenkow, J., Zaleski, C., Jha, S., Batut, P., Chaisson,
1380 M., and Gingeras, T.R. (2013). STAR: ultrafast universal RNA-seq aligner. *Bioinformatics* **29**,
1381 15–21. <https://doi.org/10.1093/bioinformatics/bts635>.

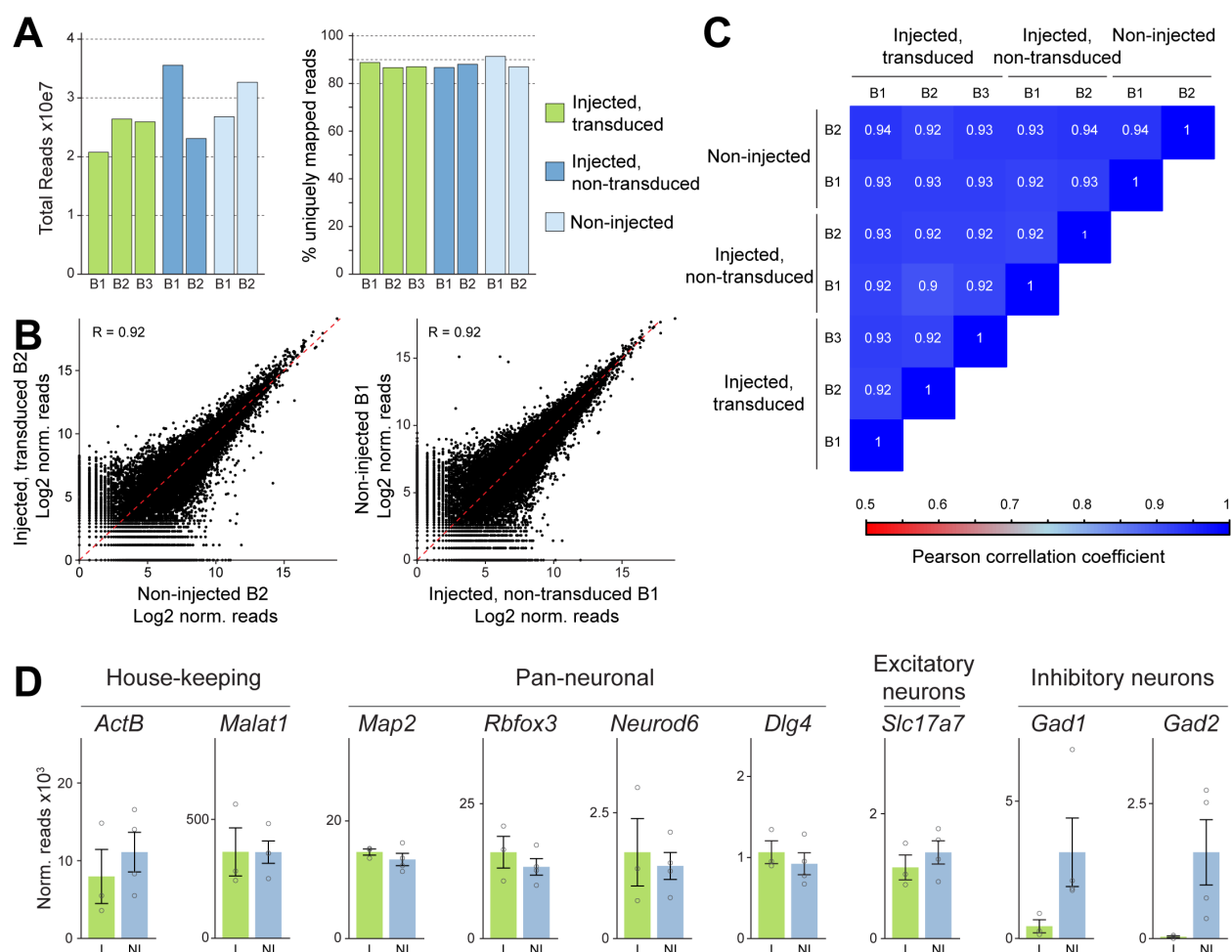
1382 121. Anders, S., Pyl, P.T., and Huber, W. (2015). HTSeq—a Python framework to work with high-
1383 throughput sequencing data. *Bioinformatics* **31**, 166–169.
1384 <https://doi.org/10.1093/bioinformatics/btu638>.

1385 122. Fang, Z., Liu, X., and Peltz, G. (2023). GSEAp: a comprehensive package for performing
1386 gene set enrichment analysis in Python. *Bioinformatics* **39**, btac757.
1387 <https://doi.org/10.1093/bioinformatics/btac757>.

Supplementary Figures

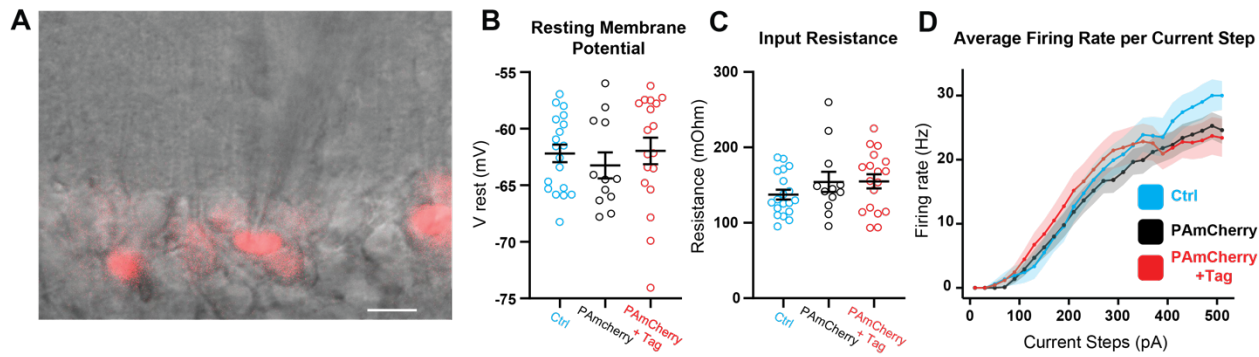


1388 **Figure S1. Additional data on 2P-NucTag.** (A) Representative average GCaMP- Ca^{2+} transients from nine CA1 PNs,
1389 vertical scale bar (50% $\Delta\text{F}/\text{F}$). (B) Left: GCaMP amplitude ($54.6\% \pm 0.3\% \Delta\text{F}/\text{F}$, $n = 8190$ cells in 9 mice). Middle: GCaMP half
1390 rise time ($0.15\text{s} \pm 0.001\text{s}$, $n = 7797$ cells in 9 mice). Right: GCaMP half decay time ($0.44\text{s} \pm 0.003\text{s}$, $n = 8282$ cells in 9 mice, 940
1391 nm excitation, See methods for cell exclusion criterion). Boxplots show the 25th, 50th (median), and 75th quartile ranges,
1392 with the whiskers extending to 1.5 interquartile ranges below or above the 25th or 75th quartiles, respectively. Outliers
1393 are defined as values extending beyond the whisker ranges. (C) Left: *in vivo* 3D visualization of the entire field of
1394 view (FOV). Middle: subset of *in vivo* 3D visualization. Right: representative cell from *in vivo* 3D visualization. (D)
1395 Left: *ex vivo* confocal 3D visualization of entire FOV. Middle: subset of *ex vivo* 3D visualization. Right: representative
1396 cell from *ex vivo* 3D visualization. C and D are corresponding to Figure 1F.

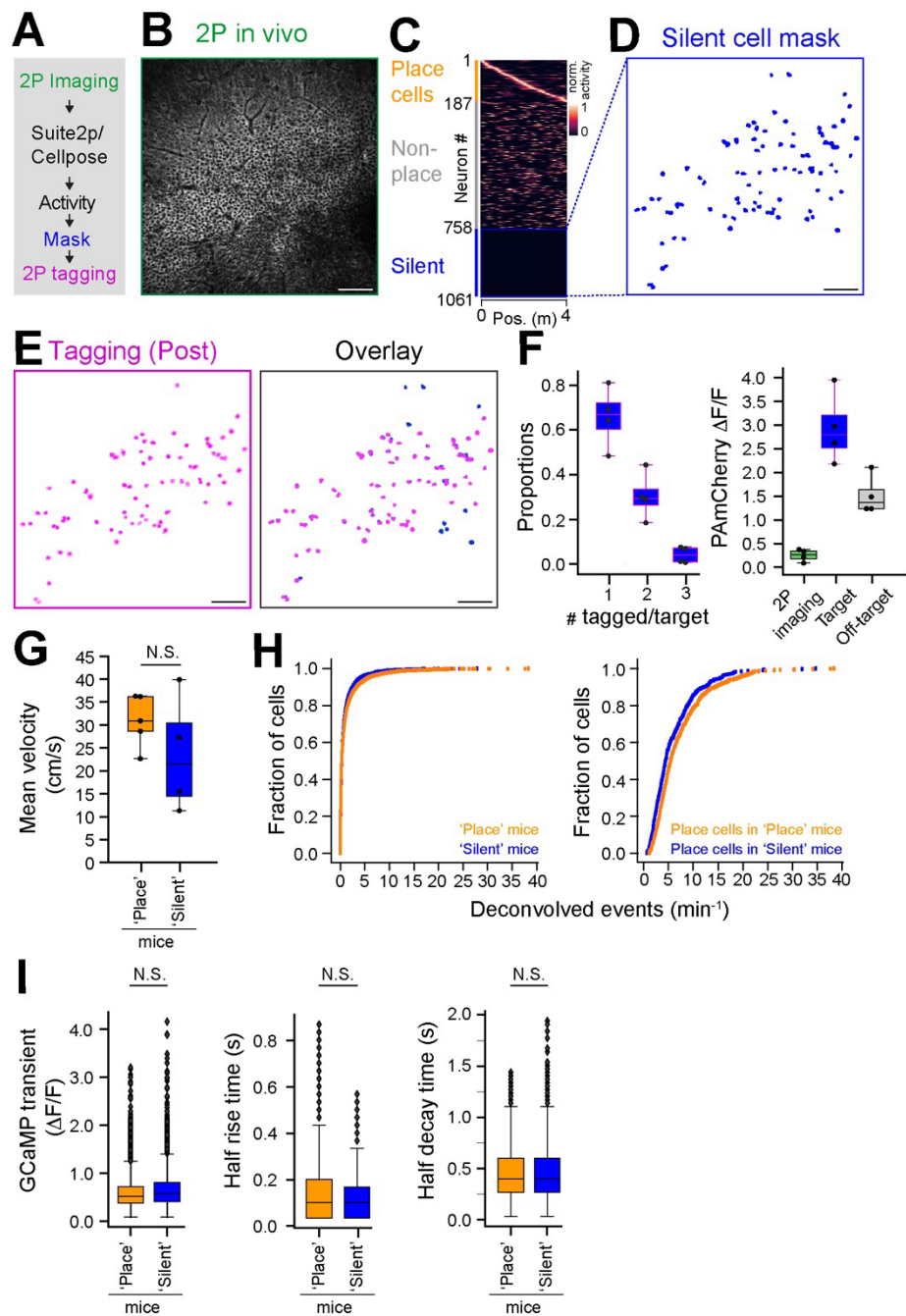


1397
1398
1399
1400
1401
1402

Figure S2. Meso-seq on hippocampal CA1 pyramidal neurons with 2P-NucTag construct. (A) Total reads and percentage of uniquely mapped reads from all libraries (B = biological replicate). **(B,C)** Pearson-correlations of all pair-wise comparisons of the expression levels of all expressed genes in the 7 libraries. **(B)** Two example comparisons. **(C)** Correlation coefficients of all comparisons (B = biological replicate). **(D)** Expression values of example genes in non-transduced neurons (NI = pool of “Non-injected” and “Injected, non-transduced”) and transduced neurons (I = “Injected, transduced”) (error-bars = SEM).

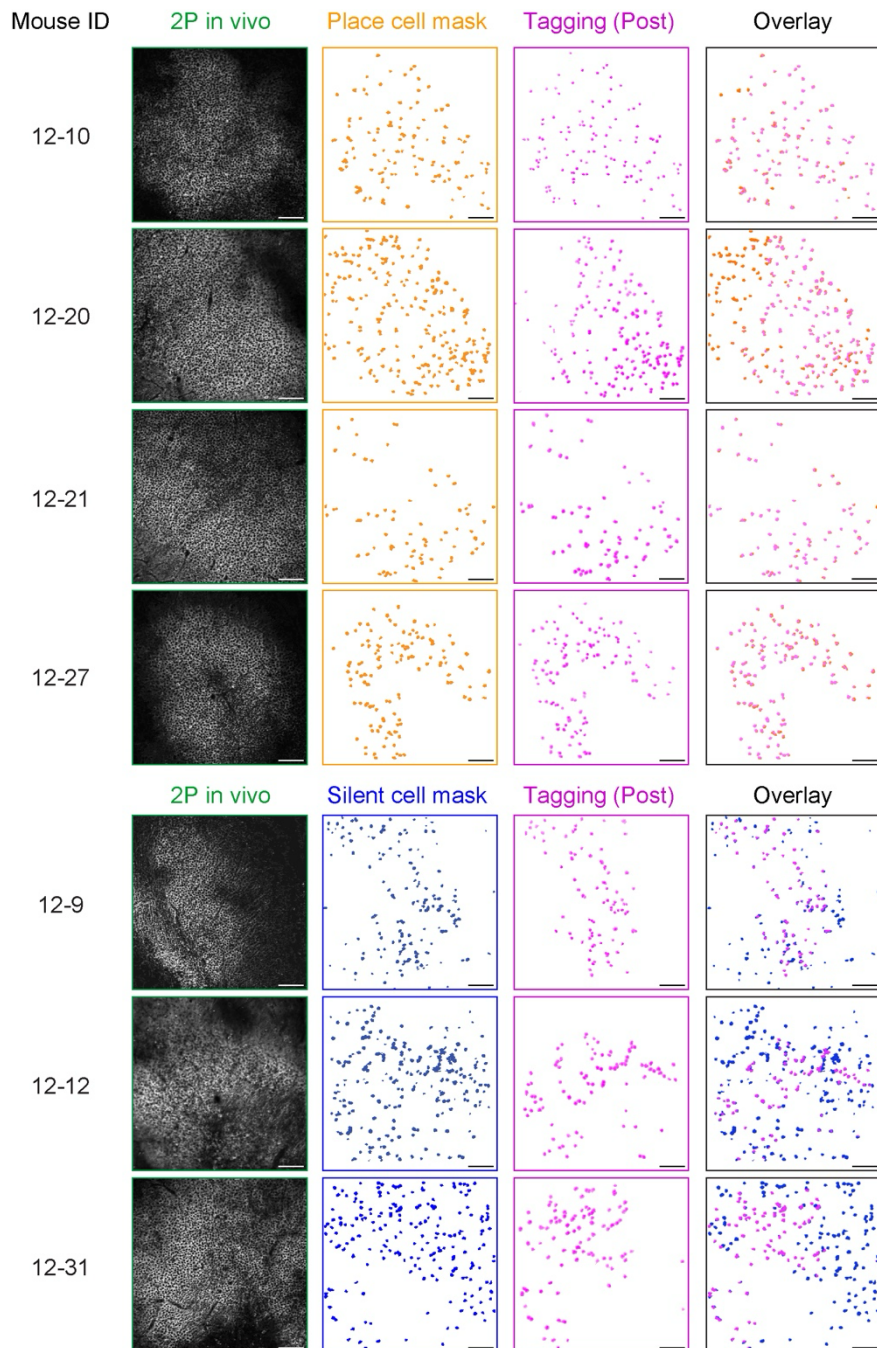


1403 **Figure S3. The 2P-NucTag construct does not alter the intrinsic properties of the CA1 pyramidal neurons. (A)**
1404 Representative image of CA1 pyramidal neurons with (red fluorescence) and without photoactivation during whole
1405 cell patch clamp recording. Scale bar: 10 μ m. **(B,C)** Quantified data of Resting membrane potential and Input
1406 resistance in CA1 excitatory neurons. Blue - control neurons (*Ctrl*), recorded in CA1 of the contralateral non-infected
1407 hemisphere. Black- are the neurons recorded from the infected hemisphere but have not been phototagged
1408 (*PAmCherry*). Red (*PAmCherry+Tag*) are the phototagged neurons (*Ctrl* n = 19 cells from 7 mice; *PAmCherry* n =
1409 12 cells from 8 mice; *PAmCherry+Tag* n = 18 cells from 7 mice; Statistics Kruskal-Wallis test with post-hoc Dunnett's
1410 T3 multiple comparisons test: no statistically significant differences were observed). **(D)** Average firing rate per
1411 current step (F-I curve) in each condition. (error bars represent SEM in all data panels).

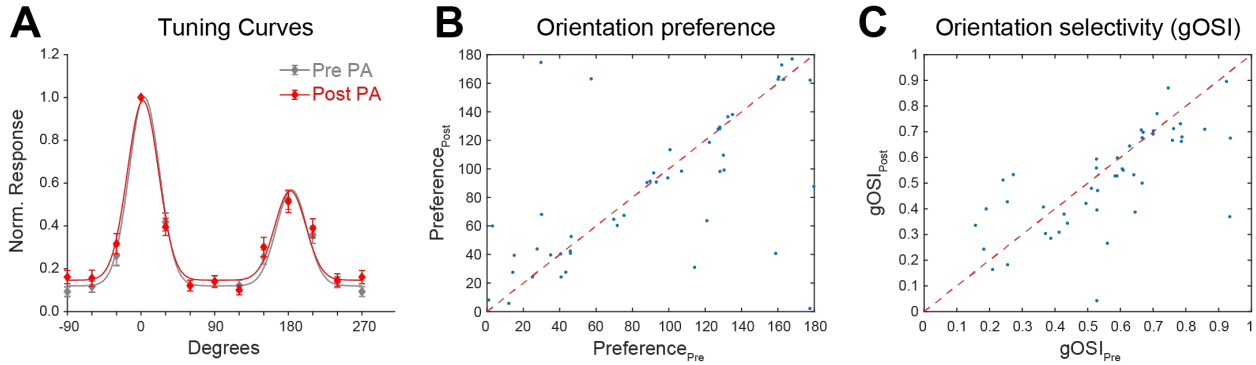


1412 **Figure S4. *In vivo* 2P-NucTag of silent cells.** (A) Pipeline for two-photon (2P) phototagging of functionally identified
 1413 ‘silent’ neurons in CA1 during VR spatial navigation (as in *Figure 1B*). (B) Example 2P imaging field of view (FOV)
 1414 of GCaMP in the CA1 pyramidal layer from a mouse with “silent” cells targeted. Scale bar: 100 μ m. (C) CA1PNs
 1415 detected with Suite2p/Cellpose in the FOV shown in *B*. (D) Spatial mask (blue) of identified ‘silent’ cells from the
 1416 FOV in *B*. Scale bar: 100 μ m. (E) Left: PAmCherry fluorescence (magenta) of tagged nuclei after 2P phototagging.
 1417 Right: overlay of spatial masks of identified CA1PNs and tagged nuclei for the FOVs in *D* and *E*. Note that we only
 1418 tagged a subset of silent cells present in the FOV. Scale bar: 100 μ m. (F) Left: Proportion of single, double, and triple-
 1419 tagged nuclei following phototagging of a single silent cell. Right: relative PAmCherry fluorescence change for non-
 1420 tagged cells in the FOV after 2P imaging (green), after 2P phototagging of targeted silent cell nuclei (blue) and off-
 1421 target nuclei (gray, n = 4 mice). (G) Average velocity of the mice during virtual reality navigation task (Mann-Whitney
 1422 U test, p-value = 0.286). (H) Left: deconvolved events per minute from all cells across all mice from 2P GCaMP-

1423 Ca²⁺imaging (averaged across mice, n = 5 ‘Place’ mice, n = 4 ‘Silent’ mice, Mann-Whitney U Test, p-value = 0.28).
1424 Right: deconvolved events per minute from place cells across all mice (averaged across mice, place n = 5, silent n =
1425 4, Mann-Whitney U Test, p-value = 0.90). (I) Left: GCaMP transient amplitude of all cells between groups (averaged
1426 across mice, n = 5 ‘Place’ mice, n = 4 ‘Silent’ mice, Mann-Whitney U Test, p-value = 0.14), Middle: GCaMP half
1427 rise time of all cells between groups (averaged across mice, n = 5 ‘Place’ mice, n = 4 ‘Silent’ mice, Mann-Whitney U
1428 Test, p-value = 0.14), Right: GCaMP half decay time of all cells between groups (averaged across mice, n = 5 ‘Place’
1429 mice, n = 4 ‘Silent’ mice, Mann-Whitney U Test, p-value = 0.81). Boxplots show the 25th, 50th (median), and 75th
1430 quartile ranges, with the whiskers extending to 1.5 interquartile ranges below or above the 25th or 75th quartiles,
1431 respectively. Outliers are defined as values extending beyond the whisker ranges.

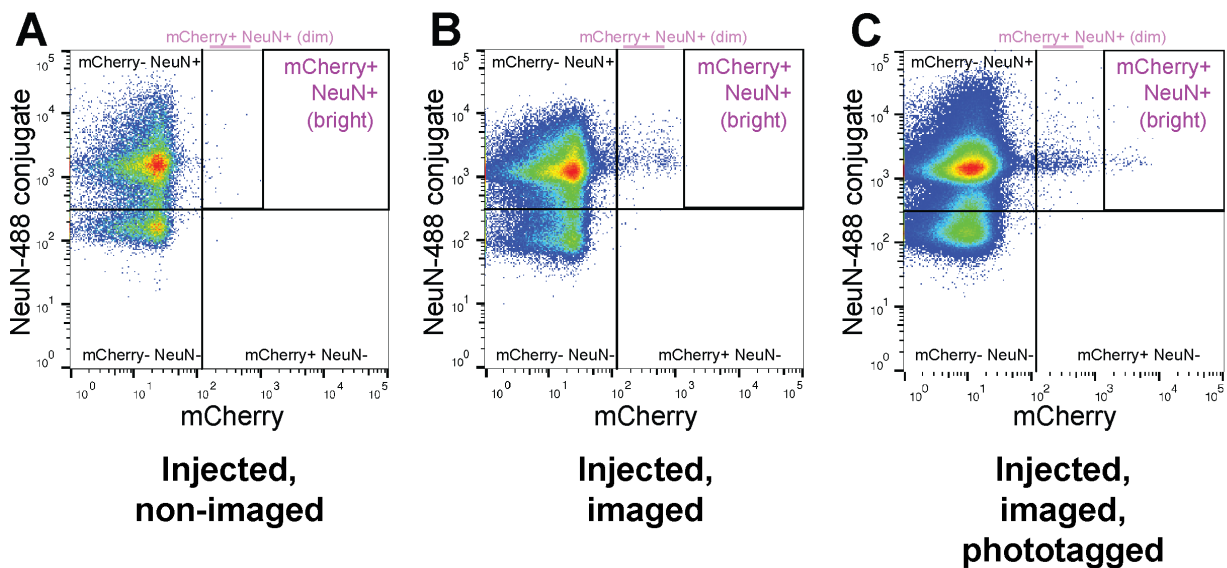


1432 **Figure S5. Additional data on phototagging.** From left to right by column: animal ID (animals in *Figure 2* and
1433 *figure S2* are not shown here), *in vivo* two-photon (2P) imaging fields of view (FOVs), functionally defined masks
1434 (orange for place cells and blue for silent cells), PAmeCherry fluorescence (magenta) of tagged nuclei after 2P
1435 phototagging and overlay of spatial masks from identified CA1PNs and tagged nuclei for the respective FOV in the
1436 same row. Note that we only tagged a subset of silent cells present in the FOV in 'Silent' mice, in order to approximate
1437 the number of phototagged place cells in 'Place' mice. Scale bar: 100 μ m.



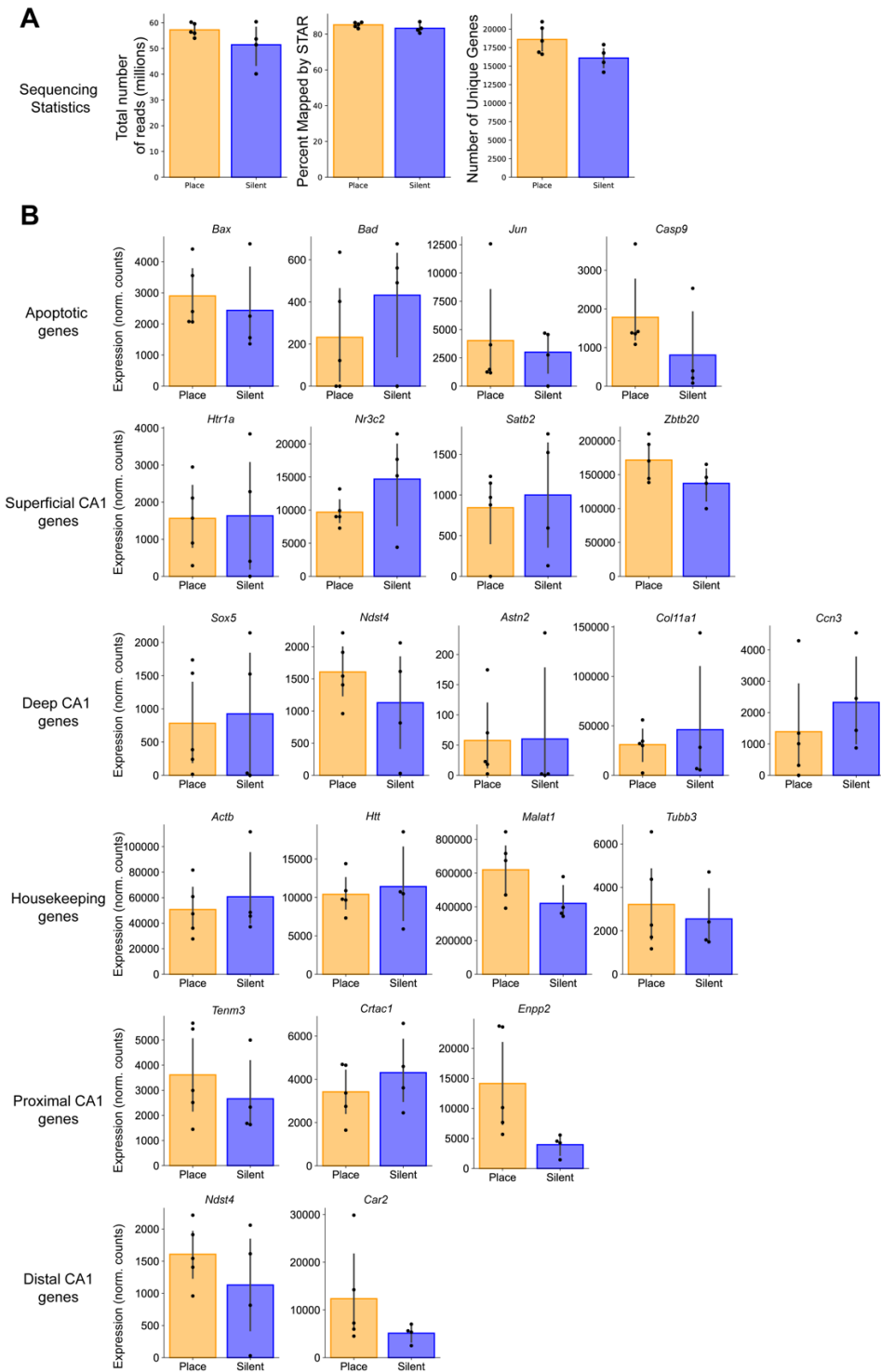
1438
1439
1440
1441
1442
1443

Fig. S6. Orientation tuning of visually responsive neurons in V1 before and after photoactivation. (A) tuning curve for visually responsive neurons before and after photoactivation (Gray – before photoactivation, Red – after photoactivation). Line - normalized double-gaussian-fitted population averages (B) Orientation preference visually responsive neurons before and after photoactivation. (C) Orientation selectivity before and after photoactivation. (Error bars represent SEM in all data panels).

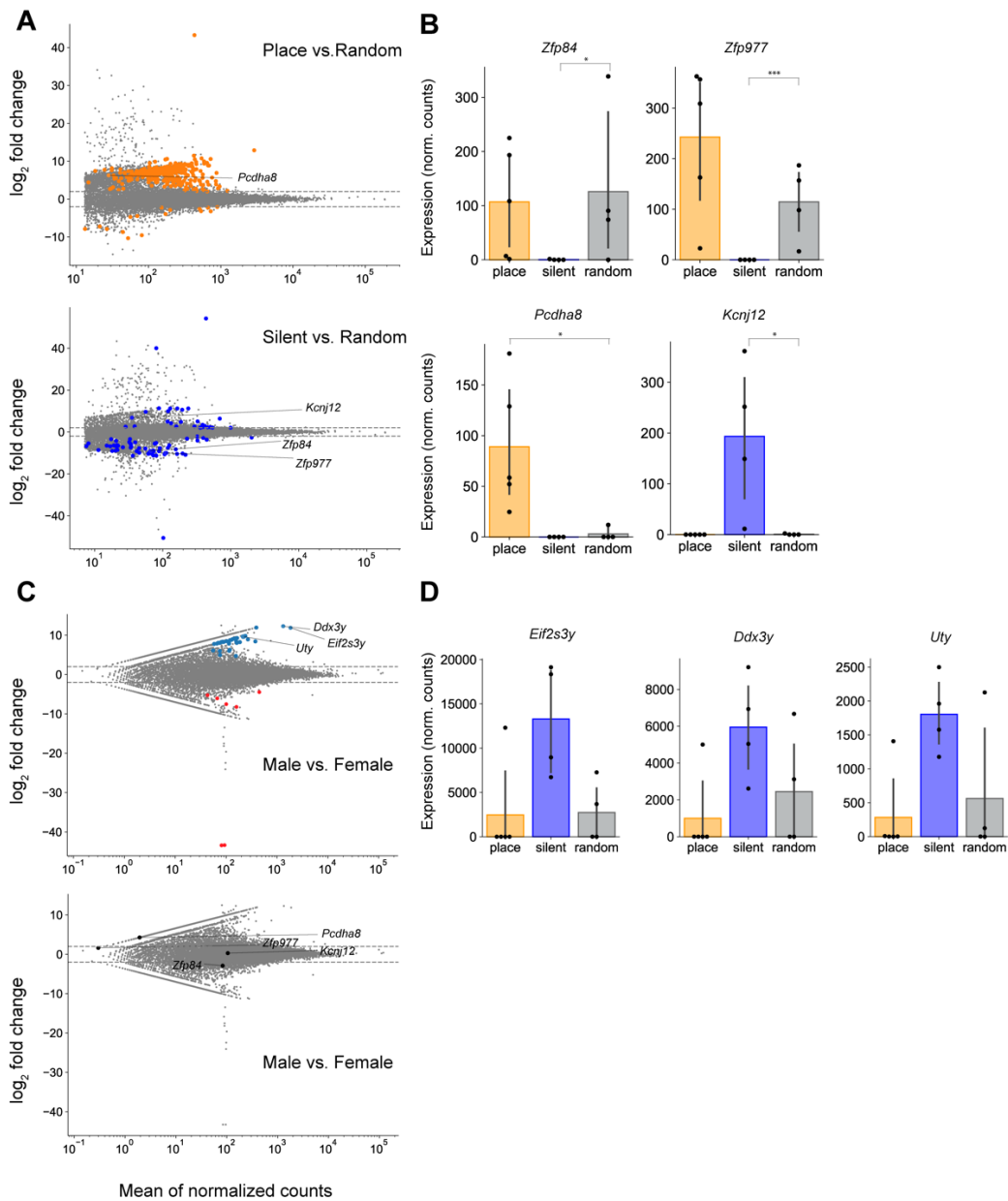


1444
1445
1446
1447

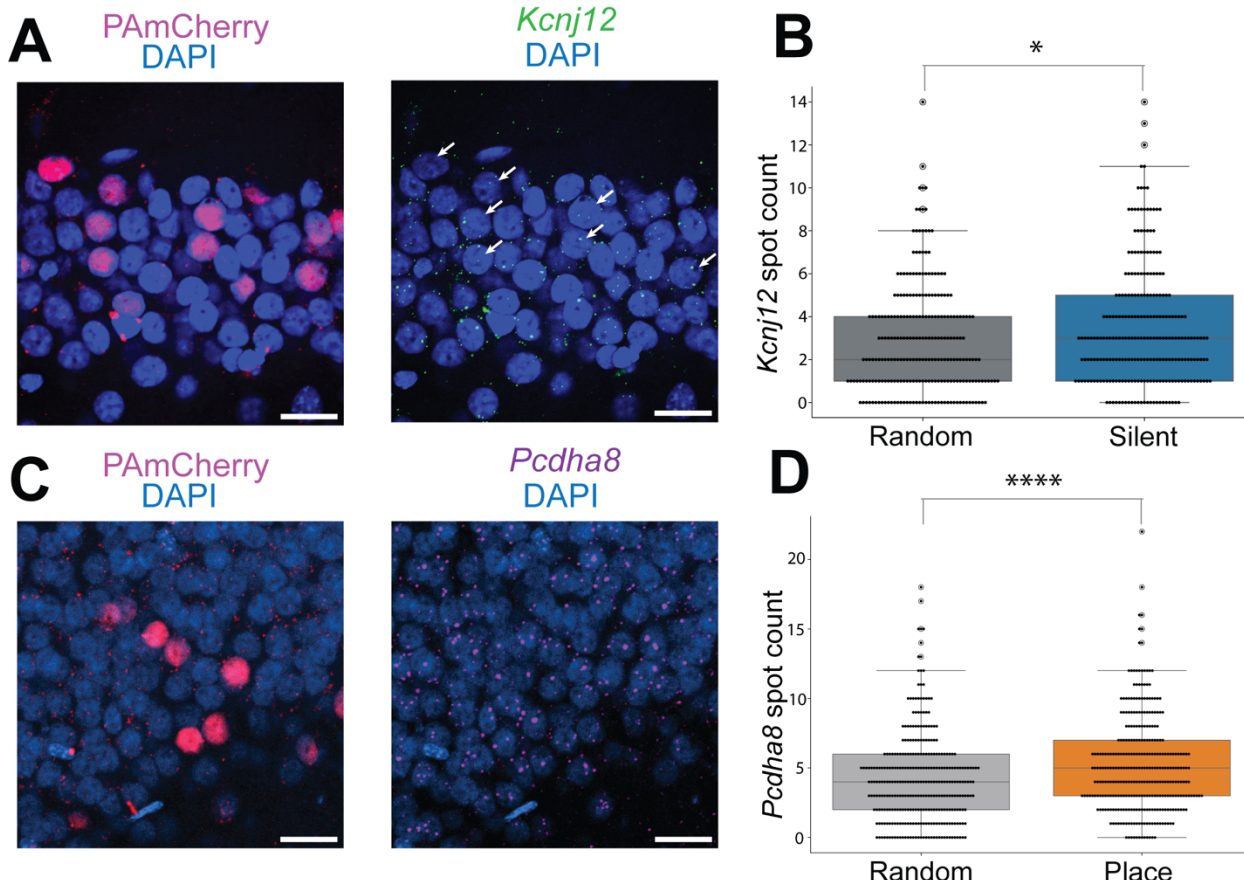
Figure S7. FACS Gating based on mCherry fluorescence. (A) representative FACS graph for samples that were injected but not imaged. (B) samples that were injected and imaged. (C) samples that were injected, imaged, and phototagged.



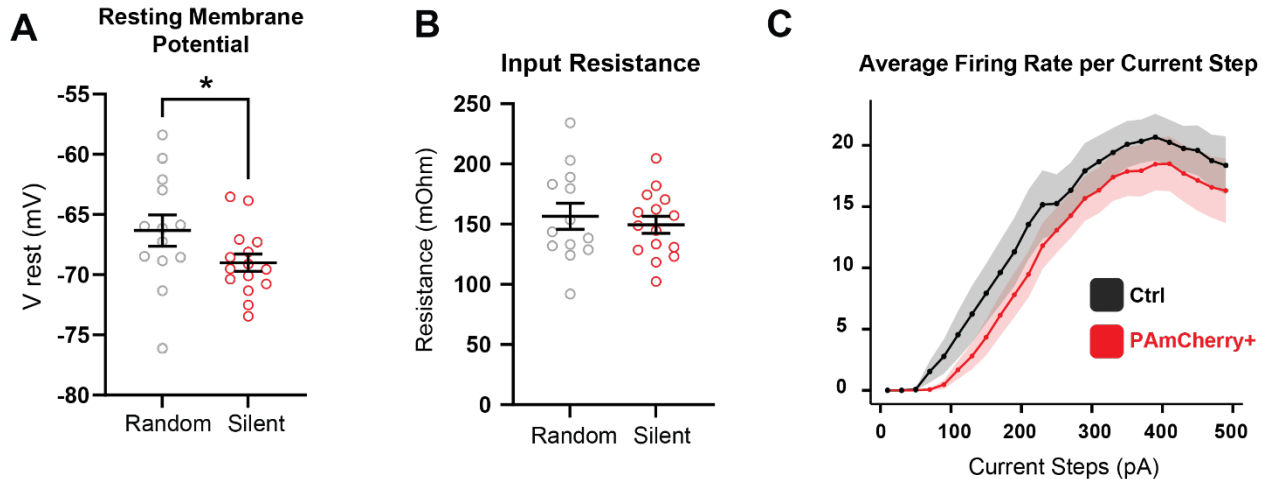
1448 **Figure S8. Additional data on transcriptomics analysis of place and silent cells.** (A) Sequencing statistics for all
1449 'place' and 'silent' cell samples. Total number of reads - 40 to 60 million reads, 54.64 ± 2.09 , $n = 9$. Percent mapped
1450 by STAR - 80.58 to 86.92%. 84.33 ± 0.73 . Number of unique genes - 14176 to 20990, 17486 ± 714 . (B) Normalized
1451 counts for groups of genes plotted for 'place' versus 'silent'. Here we show that gene expression of apoptotic genes,
1452 superficial CA1 genes, deep CA1 genes, housekeeping genes, proximal CA1 genes, and distal CA1 genes are not
1453 different between the two groups (FDR adjusted p-value. * <0.05 , ** <0.001 , *** <0.001 , PyDeSeq2. All comparisons
1454 in this figure are not significant).



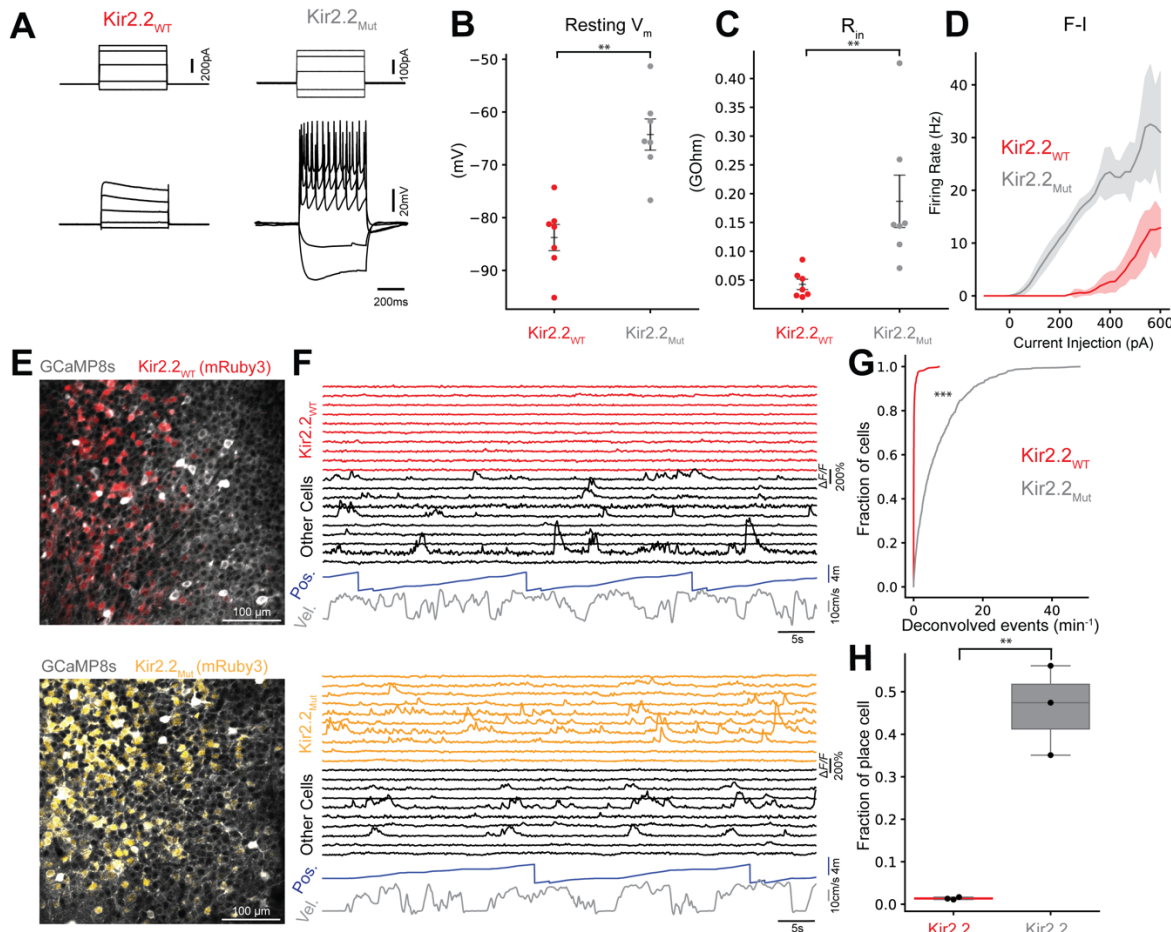
1455 **Figure S9. Additional data on transcriptomics analysis of place and silent cells.** (A) Top: MA plot of 'place'
1456 versus 'random'. Differentially expressed genes (DEGs) are labeled in orange. Bottom: MA plot of 'silent' versus
1457 'random'. DEGs are labeled in blue. Both: DEGs that are common for 'place' versus 'random' were highlighted and
1458 labeled. (B) Normalized counts for 4 example genes that are significantly differentially expressed across comparisons
1459 (FDR adjusted p-value. * <0.05 , ** <0.001 , *** <0.001 , PyDeSeq2. Showing here a comparison of 'place' versus
1460 'random' or 'silent' versus 'random'. 'Place' versus 'silent' comparisons were shown in Figure 3). (C) MA plot of
1461 male versus female for the 'random' dataset. Top: Y-linked genes that are differentially expressed between sex are
1462 highlighted and labeled. Bottom: same four genes in panel A and B are highlighted and labeled. They are not
1463 differentially expressed between sex (FDR adjusted p-value. * <0.05 , ** <0.001 , *** <0.001 , PyDeSeq2. Otherwise,
1464 comparisons are not significant). (D) Normalized counts for 3 example DEGs between male and female.



1465 **Figure S10. Spatial distribution of selected gene transcripts.** (A) Left: Confocal horizontal image showing tagged
1466 silent cells expressing PAmCherry (red with nuclei counterstained by DAPI (blue). Scale bar: 20 μ m. Right:
1467 Confocal image of the same tagged tissues as in (A), hybridized with a probe for *Kcnj12* transcripts (green) using
1468 RNAScope Multiplex Assay v2. Nuclei are counterstained with DAPI (blue). Scale bar: 20 μ m. For images shown in
1469 A&B, red mCherry image was obtained at 20x zoom pre-RNAScope; blue DAPI channel and green *Kcnj12*
1470 channels were obtained at 20x zoom post RNAScope. (B) Box plot comparing the expression levels of *Kcnj12* in
1471 tagged cells (n=247, n=3 mice, median=3, IQR=4) and randomly selected non-tagged cells (n=247, n=3 mice,
1472 median=2, IQR=3). Mann-Whitney U Test, p-value = 3.16e-2). (C) Left: Confocal horizontal image showing tagged
1473 place cells expressing PAmCherry (red with nuclei counterstained by DAPI (blue). Scale bar: 20 μ m. Right:
1474 Confocal image of the same tagged tissues as in (A), hybridized with a probe for *Pcdha8* transcripts (magenta) using
1475 RNAScope Multiplex Assay v2. Nuclei are counterstained with DAPI (blue). Scale bar: 20 μ m. (D) Box plot
1476 comparing the expression levels of *Pcdha8* in tagged cells (n=321, n=3 mice, median=5, IQR=4) and randomly
1477 selected non-tagged cells (n=321, n=3 mice, median=4, IQR=4). Mann-Whitney U Test, p-value = 1.58e-4).
1478 Boxplots show the 25th, 50th (median), and 75th quartile ranges, with the whiskers extending to 1.5 interquartile
1479 ranges below or above the 25th or 75th quartiles, respectively. Outliers are defined as values extending beyond the
1480 whisker ranges.

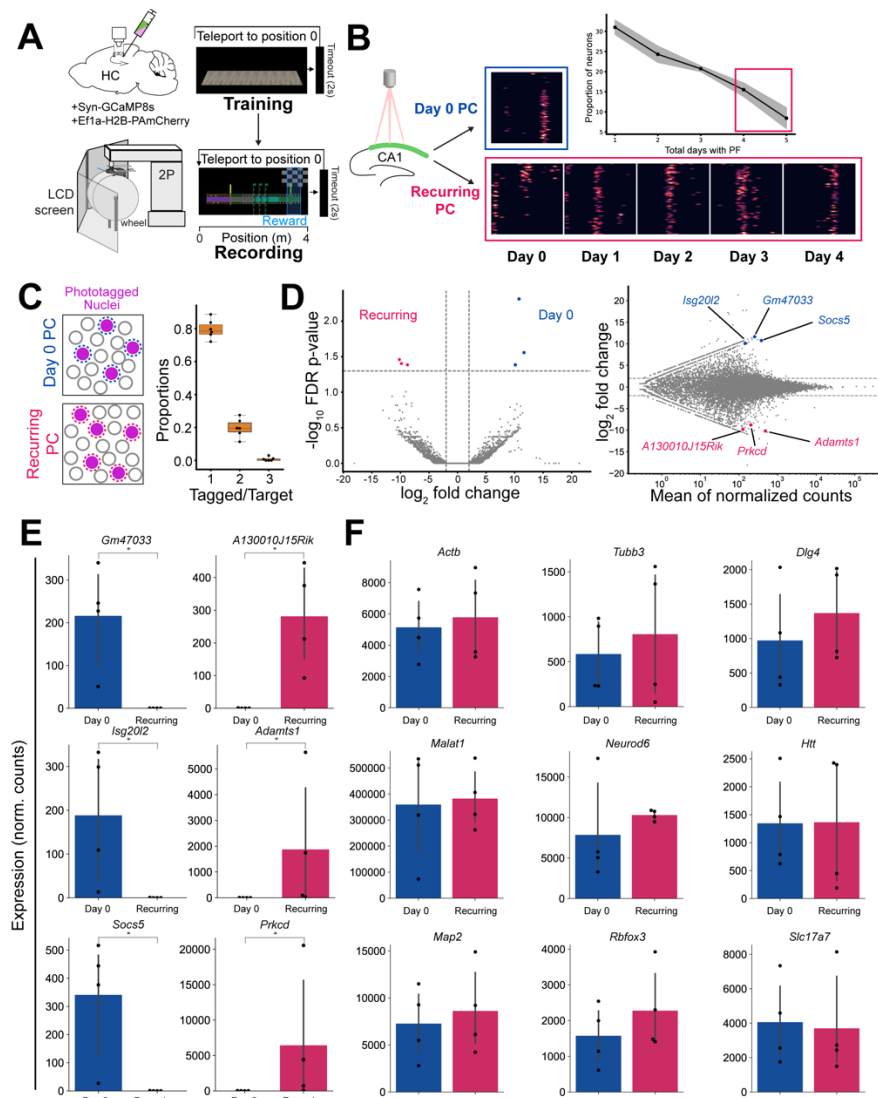


1481 **Figure S11. Silent cells display a decrease in resting membrane potential.** (A,B) Quantified data of Resting
1482 membrane potential and Input resistance in Random (non-silent, *Ctrl*) and silent (PAmCherry+) CA1 PNs (Random
1483 n = 19 cells from 4 mice; Silent n = 12 cells from 4 mice). (Mann-Whitney U test. Resting Membrane Potential: p-
1484 value=0.0401; Input Resistance: p-value=0.6832; * p<0.05). (C) Average firing rate per current step in each condition.
1485 (Error bars represent SEM in all data panels).



1486
1487
1488
1489
1490
1491
1492
1493
1494
1495
1496
1497
1498
1499
1500
1501
1502
1503
1504
1505
1506
1507

Figure S12. Ectopic expression of Kir2.2 silences CA1 neurons and reduces place cell percentage. (A) Representative traces of current (top) and voltage (bottom) as recorded in current clamp mode from cells that express either Kir2.2_{WT} or Kir2.2_{Mut}. Cells that express Kir2.2_{WT} show less action potentials despite higher current injections (current scale bar left: 200pA, right: 100pA). (B,C) Quantified data of resting membrane potential (B) and input resistance (C) in Kir2.2_{WT} and Kir2.2_{Mut} cells (Kir2.2_{WT} n = 7 cells from 2 mice; Kir2.2_{Mut} n = 7 cells from 2 mice). (Mann-Whitney U test. Resting Membrane Potential: p-value=0.001; Input Resistance: p-value=0.001). (D) Average firing rate per current step in each condition. (E) Representative 2P imaging field of view (FOV) of GCaMP and Kir2.2 channels in the CA1 pyramidal layer. Top: mouse is injected with AAV-hSyn-GCaMP8s, AAV-hSyn-FLEX-Kir2.2_{WT}-mRuby3 and AAV-hSyn-Cre to express GCaMP and sparse expression of Kir2.2_{WT}. Gray: GCaMP; Red: Kir2.2_{WT}. Bottom: mouse is injected with AAV-hSyn-GCaMP8s, AAV-hSyn-FLEX-Kir2.2_{Mut}-mRuby3 and AAV-hSyn-Cre to express GCaMP and sparse expression of Kir2.2_{Mut} as a control against Kir2.2_{WT}. Gray: GCaMP; Orange: Kir2.2_{Mut}. Scale bars: 100 mm. (F) Representative traces of dF/F, position and velocity of 2P recording during spatial navigation. For both top and bottom plots: top 10 traces are from cells that are infected with either Kir2.2_{WT} or Kir2.2_{Mut}, bottom 10 traces are from cells in the same recording field of view but are not infected with either Kir2.2 AAVs. Note for overexpression of Kir2.2_{WT}, other cells in the recording FOV are not affected by the channel overexpression and still exhibit normal calcium transients, and Kir2.2_{Mut} control cells still show normal activity. (G) Deconvolved events per minute from all cells across all mice that are infected with either Kir2.2 AAVs (n = 345 Kir2.2_{WT} cells from 3 mice, n = 620 Kir2.2_{Mut} cells from 3 mice, Mann-Whitney U Test, p-value = 1.74e-119). (H) Fraction of place cells in all cells from all mice that are infected with either Kir2.2 AAVs (Kir2.2_{WT} mean = 0.013, IQR = 0.003. Kir2.2_{Mut} mean = 0.462, IQR = 0.105. Unpaired t-test, p-value = 0.018). (Error bars represent SEM in all data panels).



1508
1509
1510
1511
1512
1513
1514
1515
1516
1517
1518
1519
1520
1521
1522
1523
1524
1525
1526

Figure S13. Transcriptional profiling of Day 0 and Recurring place cells. (A) Schematics of imaging and behavior setup. Mice were trained in featureless environments and recorded in a feature-rich environment. (B) Heatmaps of normalized $\Delta F/F$ activity from one sample day 0 place cell and one sample recurring place cell over 60 laps during VR navigation for either one day or across five days of recording. Upper right: quantification of proportion of neurons with respective numbers of place fields across 5 recording days (solid line: mean, shaded area: mean + s.e.m, $n = 4$ mice). (C) Left: schematics of *in vivo* photoactivated nuclei. ‘Day 0’ place cell sample and ‘Recurring’ place cell samples from different mice were collected for FACS and Meso-seq. Right: Proportion of single, double, and triple-tagged nuclei following phototagging of a single place cell. (D) Left: volcano plot of Meso-seq differential expressed gene (DEG) analysis for ‘Day 0’ and ‘Recurring’ place cells. Right: Meso-seq MA plot depicting DeSeq2 normalized gene counts versus \log_2 fold change of Day 0/Recurring place cells samples. Day 0 and Recurring place cells are similar in genetic profiles with only 6 differentially expressed genes identified. Genes that are significantly different are labeled in blue and magenta (same as above). Genes shown in panels E are highlighted and labeled in D. (significantly different genes are shown in blue and magenta. blue: enriched in ‘Day 0’ cells; magenta: enriched in ‘Recurring’ cells). (E) Bar graph showing the normalized counts for differentially expressed genes (FDR adjusted p-value. * <0.05 , ** <0.01 , *** <0.001 , PyDeSeq2. Otherwise, comparisons are not significant). (F) Bar graph showing the normalized counts for genes that are not differentially expressed. Boxplots show the 25th, 50th (median), and 75th quartile ranges, with the whiskers extending to 1.5 interquartile ranges below or above the 25th or 75th quartiles, respectively. Outliers are defined as values extending beyond the whisker ranges.

Table 1

Mouse	Sex	Group	Place #	Silent #	Active Non-Place #	Mask #	Tag #
12-10	Male	Place	119	208	1754	119	112
12-20	Female	Place	250	470	1232	218	168
12-21	Female	Place	89	1040	701	74	73
12-27	Female	Place	132	547	548	119	119
12-37	Female	Place	126	290	1440	119	115
12-9	Male	Silent	9	152	655	152	87
12-12	Male	Silent	28	230	287	230	89
12-31	Male	Silent	129	305	1238	200	97
12-34	Male	Silent	187	303	571	113	79

1527 **Supplementary Movie 1. Phototagging**

1528 Real-time movie of *in vivo* two-photon imaging and phototagging of neurons. Imaging was
1529 performed at 1040 nm to visualize change in PAmCherry fluorescence. During phototagging, the
1530 810-nm laser was scanned over target nuclei and the PMT was blanked. A frame average of 64
1531 frames was applied for resolution and clarity. Final video was edited to include scale bar and laser
1532 switches. Video time is not representative of actual recording time.

1533

1534 **Supplementary Movie 2. Registered *in vivo* and *ex vivo* image stacks**

1535 Three-dimensional rendering of registered z-stacks of *in vivo* and *ex vivo* tissue volume of the CA1
1536 pyramidal layer with phototagged nuclei. Corresponding to *Figure 1F* and *Figure S1C,D*.
1537 Magenta: PAmCherry *in vivo* (captured on Bruker 2P microscope, wavelength = 1070 nm).
1538 Orange: PAmCherry *ex vivo* (captured on A1 HD25, Nikon Instruments Inc., wavelength = 568
1539 nm)

1540

1541 **Supplementary Table 1. List of DEGs between place and silent cells**

1542 List of DEGs between place and silent cells showing log 2-fold change, mean of normalized count
1543 (baseMean), and FDR adjusted p-value. All genes in the table have an FDR-adjusted p-value less
1544 than 0.05 when comparing silent versus place cells. log2FoldChange is computed for silent versus
1545 place (positive: enriched in silent cells, negative: enriched in place cells).

1546 File: Supplementary_Table.